

1 **Micro-seismic monitoring of scaled laboratory hydraulic fracturing experiments for**
2 **different fracture propagation regimes**

3
4 **A. Butt¹, A. Hedayat¹, and O. Moradian²**

5 ¹ Department of Civil and Environmental Engineering, Colorado School of Mines, Golden, CO,
6 USA.

7 ²Department of Earth Sciences, Swiss Federal Institute of Technology (ETH), Zurich,
8 Switzerland.

9
10 Corresponding author: Awais Butt (ambutt@mines.edu)

11
12 **Key Points:**

- 13 • Tensile dominant fracturing observed for Barre granite, both for viscosity and toughness
14 dominated propagation regimes.
- 15 • A combination of fracturing mechanisms (tensile & shear) was detected as the hydraulic
16 fracture propagated away from the injection source.
- 17 • Higher b-values were obtained for toughness dominated propagation regime relative to
18 viscosity dominated propagation regime.
19

20 **Abstract**

21 While hydraulic fracturing is a widely employed process, the underlying fracturing processes are
22 not clearly understood. Scaled laboratory hydraulic fracturing experiments with seismic
23 monitoring can help with better understanding of the relationship between the generated hydraulic
24 fracture network and the induced micro-seismicity while taking into account the effect of different
25 HF parameters (injection fluid type and rate, stress conditions). In this study, hydraulic fracturing
26 experiments were performed on true-triaxially loaded Barre granite cubes, with real-time micro-
27 seismic monitoring, to identify and characterize the stimulation processes associated with the
28 viscosity and toughness dominated hydraulic fracturing propagation regimes. Water and gear oil
29 were used as the fracturing fluids. Moment tensor inversion technique was employed to determine
30 the fracture mechanisms (tensile, shear, or mixed-mode). Viscosity propagation regime
31 experiments involved higher breakdown pressures and larger injection fluid volumes relative to
32 toughness propagation regime experiments. The micro-seismicity from toughness propagation
33 regime experiments resulted in relatively larger b -value (2.35 compared to 1.62), indicating
34 dominance of small magnitude events. Overall, tensile fractures were dominant in both
35 propagation regimes (ranging from 52% to 58%), which can be attributed to the very low
36 permeability of the granite rock. These results indicate that even for a relatively impermeable rock,
37 theoretical assumptions of mode-I tensile fracturing and the scaling analysis may only be
38 applicable to the near borehole region and as the fracture propagates away from the borehole, the
39 fracturing pattern varies depending on the locally encountered conditions.

40 **Plain Language Summary**

41 Hydraulic fracturing has been employed to increase the permeability of deep energy reservoirs and
42 examples include oil and gas and enhanced geothermal systems. Different operational parameters
43 such as the injection fluid type, injection rate, and stress conditions can significantly impact this
44 rock stimulation and it is important to characterize this fracturing to estimate the efficiency of the
45 hydraulic fracturing process. This study involved laboratory hydraulic fracturing of cubic Barre
46 granite rock specimens with continuous micro-seismic monitoring using two different injection
47 fluids. The experiments performed with higher viscosity injection fluid resulted in higher failure
48 pressure and required a larger fluid volume, relative to experiments with low viscosity injection
49 fluid. For all the experiments, majority of the identified fracturing involved generation of opening
50 (tensile) fractures, particularly close to the fluid injection point. Experiment conducted with low
51 viscosity injection fluid generated larger number of low energy micro-seismic events. These results
52 indicate that for very tight rocks, the majority of damage involves opening of new fractures,
53 irrespective of the injection fluid. However, as the fracture size and parameter increase, the
54 hydraulic fracture will follow the path of least resistance and will be a combination of opening and
55 sliding (shear) fractures.

56 **1 Introduction**

57 Hydraulic stimulation techniques have been used over the past many decades to increase
58 the permeability of reservoir rocks in diverse applications which include oil and gas production,
59 geothermal systems, carbon sequestration, rock burst mitigation, and coalbed methane
60 development (Adams & Rowe, 2013; Stoeckhert et al., 2015; Watanabe et al., 2017). This
61 technique has also been utilized to measure the in-situ stress in numerous geotechnical and mining
62 projects (Amadei & Stephansson, 1997; Hamison & Fairhurst, 1969; Hayashi & Hamison, 1991;
63 Kang et al., 2018; Raaen et al., 2001).

64 The efficacy of the hydraulic fracturing (HF) operation can be predicted by estimating the
65 initiation and evolution of the propagated fracture geometry and the fracture patterns. Seismic
66 monitoring, or acoustic emission (AE) monitoring at the laboratory scale, is one of the most
67 effective methods to monitor the initiation and propagation of HF in brittle rocks (Lockner, 1993;
68 Stanchits et al., 2014). Continuous AE monitoring in the laboratory, can provide a real-time
69 manifestation of the imminent fluid-driven failure where AE source localization, which represents
70 the individual cracks during fracturing, can assist in mapping of the HF initiation and propagation
71 within a relatively small size rock specimen. This non-destructive monitoring technique have been
72 extensively used in the laboratory to monitor the HF propagation in a variety of natural rocks
73 (Goodfellow et al., 2015b; Ishida, 2001; Li & Einstein, 2019; Lockner & Byerlee, 1977; Solberg
74 et al., 1980; Stanchits et al., 2015; Zhuang et al., 2019a, 2019b; Zoback et al., 1977). The HF
75 stimulation can occur through the opening of new fractures (tensile mode), slip along the pre-
76 existing fractures (shear mode) or by a combination of these mechanisms (mixed mode). These
77 fracturing modes influence the efficiency of the stimulated reservoir; for example, tensile fractures
78 are more advantageous for easy penetration of proppants and can enhance the productivity of the
79 created HF. However, in the absence of proppants, tensile fractures may close upon the fluid
80 injection termination and in that case, shear fractures can prove to be the viable option. Also, the
81 size and geometry of the stimulated reservoir can be affected by the normal (tensile) or shear
82 dilation of the generated fracture (Amann et al., 2018). Majority of the recorded seismic data, from
83 field HF operations, points towards shear dominated mechanisms, despite the theoretical
84 predictions of tensile dominance (Maxwell, 2011a, 2011b). Therefore, to resolve this ambiguity
85 and for an efficient HF design, it is essential to accurately determine the different damage
86 mechanisms in a HF operation. Hampton et al. (2018) utilized moment tensor analysis (MTA) for
87 the characterization of the recorded AE activity during HF experiments in true triaxially loaded
88 granite blocks. The individually detected damage or crack, known as AE events, were classified
89 as tensile, shear and mixed mode (combination of tensile and shear) events. However, these AE
90 events were randomly distributed all over the specimen and it was difficult to distinguish between
91 the main HF and the non-hydraulically connected damage in the specimen. Similar
92 characterization of HF induced damage was performed by Yamamoto et al. (2019) using MTA on
93 small granitic cuboids loaded only uniaxially.

94 The laboratory scale HF studies enables one to understand and elucidate the mechanisms
95 of fluid driven fractures and provide the opportunity to measure different parameter values that are
96 unavailable from field operations. However, to correctly infer the nature behind the complex
97 processes involved, it is enormously important to make the appropriate connection between the
98 two drastically different scale operations. Neglecting this important aspect has resulted in some
99 contradicting results and have kept the community divided on the importance of the involved
100 parameters (Bunger et al., 2005). In the field, the HF propagation transitions between different
101 regimes, which depends on the variety of factors including the injection fluid properties (rate and
102 viscosity), properties of rocks and the far field stresses (Sarmadivaleh, 2012). If the energy
103 consumed in the creation of new fracture surfaces is small relative to the viscous dissipation
104 energy, viscous propagation regime (VPR) is the dominant regime. In toughness propagation
105 regime (TPR), the energy spent on new fracture surface creation is much larger than the viscous
106 counterpart (Detournay, 2004). The fracture initiation usually occurs in a TPR but rapidly
107 transitions into a VPR, while ultimately terminating in the TPR for a radial or penny-shaped HF
108 (Bunger, 2005; Bunger et al., 2005; Detournay, 2004; Mack and Warpinski, 2000). Correct scaling
109 of the physical phenomena and stability of fracture propagation are very important to mimic the

110 quasi-static processes occurring in field fracturing operations (De Pater, 1994a), which are missing
 111 in a vast majority of laboratory studies of HF. According to Detournay (2004), the value of
 112 dimensionless toughness parameter (κ) can ascertain if the propagation occurs in the VPR or TPR,
 113 depending on the time of the experiment. This is obtained using the basic HF propagation model,
 114 involving a planar crack, where the fracture propagates quasi-statically by the injection of a
 115 Newtonian fluid at a constant injection rate in opening mode being perpendicular to the minimum
 116 principal stress in an elastic medium (Detournay, 2016). This model results in a non-linear system
 117 of equations, revealing the evolution of fluid pressure, fracture width and extent with time. This
 118 dimensionless parameter can be calculated as follows:

$$119 \quad \kappa = K' \left(\frac{t^2}{\mu'^5 Q_o^3 E'^{13}} \right)^{\frac{1}{18}} \quad (1)$$

120 where $K' = \left(\frac{32}{\pi}\right)K_{IC}$, (K_{IC} = Mode-I fracture toughness of the rock); $E' = \left(\frac{E}{1-\nu^2}\right)$, (E =
 121 Young's modulus; ν = Poisson's ratio); $\mu' = 12\mu$ (μ = fracturing fluid viscosity); t = experiment
 122 time, Q_o = Rate of fluid injection. For $\kappa \leq 1$, the VPR dominates and for $\kappa \geq 3.5$, the TPR dominates
 123 (Savitski and Detournay, 2002). The assumptions for this prediction include the mobile
 124 equilibrium ($KI = KIC$) once the fracture initiates, point source for fluid injection and very small
 125 lag (difference between fracture and fluid front) relative to fracture radius. The grain size of the
 126 host rock influences the fracture toughness and dilatancy properties and may have a more
 127 significant effect for laboratory fracturing compared to the field; however, micro-structural scaling
 128 was found to be impractical, as reported by De Pater et al. (1994a,1994b) and is not considered in
 129 the present study.

130 The interest of the scientific community in crystalline rocks studies have increased
 131 considerably in recent times due to the advances in hard rock HF applications. An example is the
 132 enhanced geothermal systems (EGS) technology, where HF is used to stimulate and increase
 133 permeability of an unconventional reservoir for cost-effective heat extraction. However, since the
 134 focus of majority laboratory HF studies have been for the applications in the oil and gas industry,
 135 very limited studies can be found in crystalline rocks, and therefore, the inferences from these
 136 studies, including the scaling analysis, may or may not be applicable to the granitic rocks. The
 137 granitic rocks are quite different from the traditional sedimentary reservoir rocks, due to their
 138 variable mineral composition and are also much more affected by the experimental conditions
 139 (Zhuang & Zang, 2021). The permeability of granite formations is usually much lower relative to
 140 fractured or porous petroleum reservoir formations. In addition, out of the limited studies in low
 141 permeability granite, majority used small cylindrical rock samples with pseudo triaxial confining
 142 state (Zhuang et al., 2018, 2019a, 2019b). The subsurface rock strata are located in 3D stress
 143 conditions and experiments performed on cubic or cuboid rock specimens, loaded in all three
 144 mutually perpendicular directions, can present a better picture for understanding the mechanics of
 145 rock fracture (King et al., 2012). The results, either from the layered sedimentary rocks or small-
 146 size cylindrical granite specimens may not present an accurate picture of fracturing mechanisms
 147 experienced in high strength granite at the field scale (Cheng & Zhang, 2020).

148 The main objective of this study was the characterization and differentiation of fluid
 149 induced damage in crystalline rocks following different dominating propagation regimes, through
 150 the micro-seismic analysis. Scaled laboratory HF experiments were performed in hard transversely
 151 isotropic Barre granite cubes loaded true-triaxially with real-time micro-seismic and borehole
 152 pressure decay monitoring. An effort was made to identify the applicability and limitations of

153 scaling analysis to the low permeability granitic rocks. An advanced seismic analysis technique,
154 MTA, was also used to discover the fracturing mechanisms of the detected AE events and their
155 evolution, for different propagation regime experiments.

156

157 **2 Experimental setup**

158 2.1 Material and borehole installation

159 Hydraulic fracturing was investigated using precisely cut and polished Barre granite cubes
160 (165 mm x 165 mm x 165 mm) which represents the typical reservoir rocks encountered in
161 geothermal projects (Cornet et al., 2007; McClure and Horne, 2014a; Xie et al., 2015). This
162 medium-grained granite, with mineral grain size between 0.25 and 3 mm, was acquired from E. L.
163 Smith quarry located in the city of Barre, Vermont, USA. The density, porosity, and compressive
164 strength of Barre granite were 2654.26 kg/m³, 0.2 % and 165 MPa, respectively. Feldspar is the
165 main constituent mineral (65% by volume), followed by quartz (25% by volume) and biotite (6%
166 by volume) (Dai & Xia, 2013). Like most granites, Barre granite has a clear anisotropy with three
167 mutually perpendicular cleavages. These planes of weaknesses, with different densities of micro-
168 cracks and minerals, were identified by obtaining the compressional (P-) wave velocities in all
169 three directions. These velocity directions, highest (~4500 m/s), intermediate (~4000 m/s) and
170 slowest (~3500 m/s), were termed as the hard-way, grain, and rift plane, respectively. Tensile
171 strength, mode-I fracture toughness and modulus of elasticity of Barre granite varies from 10-15
172 MPa, 1.14-1.89 MPa. (m)^{1/2} and 32-56 GPa, respectively, along the weakest and strongest planes
173 (Li & Einstein, 2019; Li et al., 2019; Nasserli et al., 2006; Sano et al., 1992). The rift plane was
174 kept perpendicular to σ_3 -direction, to encourage fracturing in the preferred orientation. A masonry
175 drill bit was used to drill a 10 mm diameter borehole parallel to the hard way plane, up to 110 mm
176 depth. A very slow speed of the drill press ensured minimum damage in the vicinity of the
177 borehole. A stainless-steel pipe with the outer diameter of 9 mm was used to case the top 60 mm
178 section of the borehole using high strength epoxy. This arrangement provided an open HF section
179 with the length of 50 mm in the middle of the specimen (Figure 1a).

180 The importance of a well-oriented notch has been considerably emphasized upon by many
181 researchers, where the size and the direction of initial notch can significantly affect how the
182 hydraulic fracture initiates (Lhomme et al., 2005; Sarmadivaleh et al., 2013; Savic et al., 1993).
183 However, slight deviations in notch location with respect to the preferred fracture plane
184 (perpendicular to σ_3), can result in fracture initiation from a point other than the pre-existing flaw
185 (Fallahzadeh et al., 2017). Also, in the field, it is difficult to control the exact location and depth
186 of the perforations and the damage induced by the drilling process may also govern the initiation
187 of the fracture (Bunger & Lecampion, 2017). Therefore, due to uncertainty in obtaining a perfectly
188 vertical notch at a certain depth inside the small borehole in very hard Barre granite rock, the
189 hydraulic fracturing was performed without any initial notches. Instead, a high differential stress
190 ($\sigma_2 - \sigma_3$) was used to assist the initiation and propagation of fracture in the preferred direction. A
191 high deviatoric stress ($\sigma_2 / \sigma_3 = 2 - 3$) can result in a more planar and simpler hydraulic fracture
192 geometry ((Maxwell et al., 2016; Pan et al., 2020). Therefore, the maximum horizontal stress (σ_2)
193 was chosen to be 2.5 times of the minimum horizontal stress (σ_3).

194

195

196 2.2 Loading, injection, and AE setup

197 Three pairs of loading platens, each consisting of a 19 mm thick steel base plate and a 6.35
198 mm aluminum cover plate, were used to house the AE sensors used in this study. The relatively
199 soft aluminum cover plate ensured a smooth contact with the specimen surface while minimizing
200 the friction. A total of 16 AE sensors were embedded in platens that could house up to 32 sensors
201 (Figure 1b). Platens also included the same number of holes for placement of the ultrasonic
202 transducers, although not utilized in the current study. The positions of the sensors were selected
203 based on the experimental setup and the number of available sensors, expected location of the
204 damage, and the optimum arrangement for the AE detection. An additional cutout in the top platen
205 accommodated the injection assembly. Deformable spring-loaded washers were placed behind the
206 sensors, which upon loading preserved the continuous contact with the specimen surface. In
207 addition, to ensure proper coupling between the specimen and the sensors, oven-baked honey
208 (dehydrated in the oven at 100°C for 90 minutes) was used. This procedure has been successfully
209 utilized in different acoustic studies (Hedayat et al., 2012, 2014a, 2014b, 2014c, 2014d; 2018; Butt
210 et al., 2019; 2020).

211 The Teledyne ISCO 500HPx high pressure syringe pump was used to inject fluid into the
212 granitic rock. The injection pump had a volume capacity, flow range, and maximum pressure limit
213 of 507.38 ml, 1-6 - 408 ml/min, and 35 MPa, respectively. The highest viscosity fluid that could
214 be accommodated in the injection pump was 1500 cP (mPa.s) and the pressure rating of the
215 injection lines were 22.5 MPa. True-triaxial frame with three independent hydraulic pistons were
216 utilized for the loading of the blocks. The two lateral and the one vertical piston had a capacity of
217 47 MPa and 62 MPa, respectively.

218 During the HF experiment, the emitted AE signals were detected and recorded using 16
219 piezoelectric sensors and two eight-channel boards from the MISTRAS group. These miniature
220 Nano-30 sensors, with a small diameter of about 8 mm, had a resonant response of 300 KHz with
221 a good frequency response over the range of 125-750 KHz. To assist detection, the output voltage
222 of the AE sensors was either amplified by 20 decibels (dB) or 40 dB, using 2/4/6 PAC pre-
223 amplifiers, for different experiments. Initially the experiments for different propagation regimes
224 were performed with 20 dB gain only. However, it was found that the AE detected from TPR
225 experiments were not adequate for further analysis and therefore, additional experiments with 40
226 dB gain were conducted to complement those with 20 dB gain setting. Using different gain for
227 each type of experiment identified the merits and demerits of using both the high and the low gain.
228 Goodfellow et al. (2013) utilized sensors amplified by 6 dB and 40 dB in a triaxial deformation
229 experiment and discussed how by overlaying the 40 dB continuous waveform over the 6 dB
230 waveform, the loss in amplitude information can be identified. Perfect synchronization between
231 the AE signals and the borehole pressure data was achieved by recording the pressure data directly
232 in the AE system at a rate of 10 Hz. Figure 1c presents a schematic of the complete experimental
233 setup.

234 2.3 Damage localization and characterization through AE data processing

235 In this study, AE source localization and characterization were performed through the
236 procedure described in Li et al. (2019b). An accurate P-wave arrival time for each recorded AE
237 waveform was determined using the Akaike information criterion (AIC). The AE event locations
238 were determined for a minimum distance error of 5 mm using a constant velocity model of 4000
239 m/s. For seismic source characterization, different methods have been adopted in the past studies,

253 including the average frequency/rise angle method (RILEM technical Committee, 2010), first P-
254 wave polarity method (Zang et al., 1998) and the MTA method (Ohtsu, 1995). The MTA is the
255 most proficient method, which divides the determined source mechanisms into tensile, shear and
256 mixed mode (Grosse & Ohtsu, 2008) and was used in this study. A moment tensor is a
257 representation of the source of a seismic event, where it describes the deformation at the source
258 location that generates the seismic waves. In moment tensor inversion, recorded sensor data and
259 the inverse Green's function are used to determine the source moment tensor. In this study, a less
260 tedious inversion method, known as the Simplified Green's function for Moment tensor Analysis
261 (SiGMA) was used. SiGMA selected only the initial portion of the detected AE signals for arrival
262 time, amplitude, and polarity to determine the six independent moment tensor components. The
263 determined symmetric 2nd degree tensor (3x3 matrix), with six independent elements, were later
264 decomposed into eigenvalues and eigenvectors to classify the cracking mechanisms. The
265 eigenvalues of the moment tensor were represented by a combination of tensile and shear crack
266 and the decomposition was obtained as their relative ratios. Also, the eigenvector analysis of the
267 moment tensor provided the orientation of the cracks.

268 2.4 Experimental protocol

269 The experimental protocol followed for all the experiments is as follows:

- 270 • After the specimen was placed in the true-triaxial setup, the stresses on the sides of
271 the block were increased in the prearranged manner. The stresses on all the three
272 specimen sides were increased to the σ_3 stress level, simultaneously. Stress in the
273 σ_3 direction was kept constant, whereas the stresses in σ_2 and σ_1 direction were
274 increased to σ_2 stress level. Ultimately σ_1 was then increased to the selected stress
275 value.
- 276 • After tightening all the connections, a brief constant pressure test was performed to
277 identify any unlikely leakage in the complete system. Pressure was increased
278 stepwise to ~7 MPa in ten steps of ~0.7 MPa for 30 sec each. This value of injection
279 pressure (7 MPa) is much below the expected value of BP and therefore cannot
280 cause any damage in the very strong and relatively impermeable Barre granite
281 block.
- 282 • After the important pre-check, the pressure in the borehole was reduced to 0.7 MPa,
283 which served as the starting point for all the experiments, ensuring the saturation of
284 the borehole and the injection lines.
- 285 • Fluid flow at a pre-selected constant rate from the injection pump commenced
286 almost simultaneously with the activation of the AE data acquisition system. When
287 the pressure started to rise at almost a linear rate, an effort was also made to reduce
288 the system compressibility by limiting the amount of fluid flux entering the fracture
289 at initiation point, which assisted in the stable propagation of fracture (Li &
290 Einstein, 2019; Liu et al., 2020; Sarmadivaleh et al., 2013). The opening at the valve
291 control (Figure 1c) was reduced which ensured minimal fluid flux entering the open
292 borehole section, which assisted in preventing the unstable and sudden failure.
- 293 • The experiment was continued after the BP of the specimen while acquiring AE
294 data and the test was only stopped after the injection pressure appeared to be

295 constant for a considerable period and without any substantial AE activity (less than
296 2-3 AEs in a five second interval).

297 • The pistons were retracted in the similar manner; σ_1 reduced to σ_2 stress value and
298 then both reduced to σ_3 stress and lastly all pistons were retracted to zero stress
299 positions.

300 • After removing the injection assembly, the block was cleaned of any excess
301 injection fluid and the fractured rock was visually inspected for any propagated
302 fractures along the boundaries of the specimen.

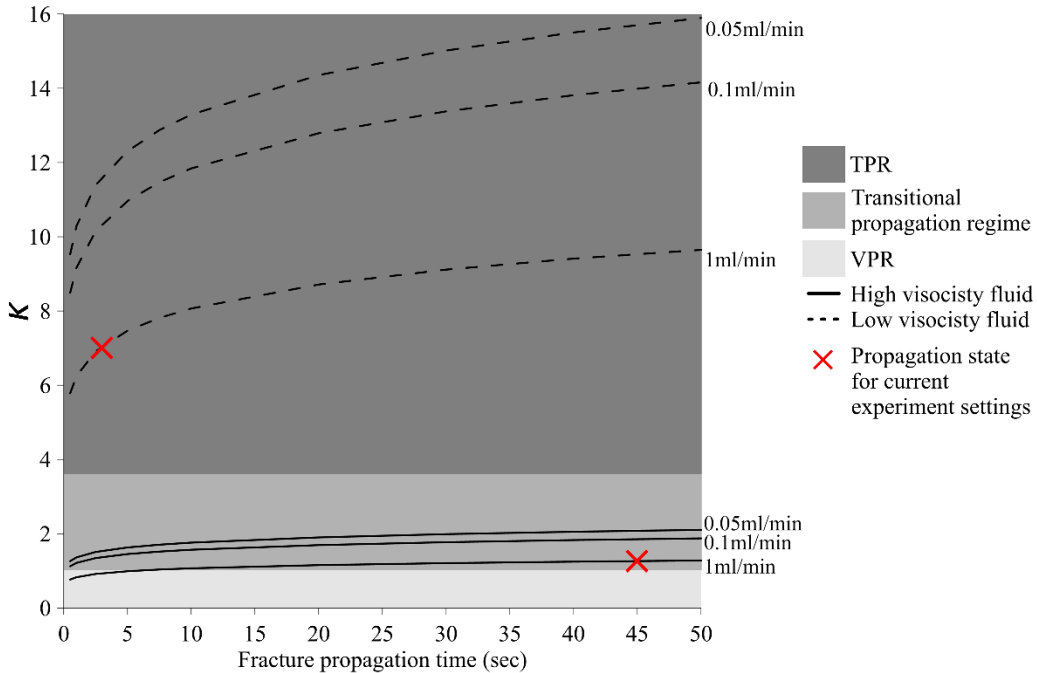
303

304 **3 Experimental results**

305 3.1 Scaling analysis

306 Scaling laws predict the laboratory experimental settings, through which the fracture
307 propagation regime in the laboratory can be analogous to that in the field. The required inputs for
308 scaling analysis are the hydro-mechanical properties of the rock, confining stress and the injection
309 fluid's rate and viscosity. The rift (weakest) plane material properties of the Barre granite were
310 used in the scaling analysis. Injection fluids with drastically different viscosities, water (1 cP) and
311 gear oil (1450 cP), were used for the HF experiments. This gear oil was used keeping in view the
312 highest viscosity limitation of the available injection pump available. However, this relatively
313 mediocre viscosity gear oil prevented the large fluid lag length, which should be avoided either
314 through lowering the viscosity of injection fluid or increasing the confining stress (Garagash &
315 Detournay, 2000). Also, system compressibility can severely impact the HF experiment, in case
316 of a remarkably high viscosity fluid or injection rate (Lecampion et al., 2017). Both the injection
317 fluids were injected at a constant injection rate of 1 ml/min. The pressure rating of the injection
318 lines (22.5 MPa) prohibited testing with higher injection rates for the gear oil, which may have
319 resulted in breakdown pressures (BP) higher than those permitted by the injection lines. In the
320 scaling analysis, experiment time or the fracture propagation time is the time from the fracture
321 initiation to the end of fracture propagation (fracture reaching the boundaries of the specimen in
322 laboratory experiments). It is imperative to determine this exact period from the fracture initiation
323 to fracture arriving at the boundaries of the laboratory specimen, as it will determine the value of
324 κ and the state of HF. Most of the laboratory studies determine this experiment time from the
325 borehole pressure decay curve alone; however, the minor changes in pressure due to fluid flow in
326 the generated fractured may make it difficult to estimate and other supplemental techniques, like
327 AE monitoring, can be useful in finding this time period.

328 The values of dimensionless toughness parameter (κ), Eq. (1), with different experimental
329 conditions (different injection fluids, injection rates and fracture propagation times) are presented
330 in Figure 2. Instead of the traditional method of fracture propagation time determination through
331 the borehole pressure analysis, in this study, the fracture propagation time was determined by
332 monitoring the AE data and the minimum horizontal stress (σ_3) (see section 4.1 for more details).
333 Based on the propagation times determined after the experiments, specific κ values were
334 determined for experiments with different injection fluids performed for this study. The summary
335 of the experimental parameters and the scaling analysis are presented in Table 1.



336

337 **Figure 2.** The dimensionless toughness parameter, κ , determined for different experimental
 338 settings and fracture propagation times and different injection rates. High viscosity injections are
 339 presented in solid lines and low viscosity injections in dashed lines. The points in the graph (X)
 340 indicates the determined state of the HF operation for experimental settings used in this study. A
 341 κ value of 1.27 corresponded to an almost viscosity dominated propagation regime, whereas a
 342 value of 7.0 resulted in the toughness dominated propagation regime

343

344

345

346

3.2 Well-bore pressure decay analysis and AE events

347

348

349

350

351

352

353

354

$$\text{Normalized time} = \frac{\text{Experiment time} - \text{BP time}}{\text{Total time}} \quad (2)$$

355

356

357

358

359

where BP time is time at breakdown and total time is the time from the start of the test until the borehole pressure reached a constant value, following the rock breakdown. Positive values of normalized time indicate the post-breakdown stage of the experiment while negative values indicate the pre-breakdown stage. Figure 3c presents the pressure evolution against the normalized time for a pair of experiments each for VPR and TPR experiments. Figure 4 presents the detected

360 AEs and the cumulative AEs against the borehole pressure evolution for the VPR and TPR
 361 experiments, respectively. The AEs amplitude from the 40-gain experiments were divided by 10
 362 for comparison with the 20-gain experiments. Fracture initiation was detected following the
 363 increase in the number of detected AEs. BP was the highest pressure recorded in a particular
 364 experiment.

365 **Table 1.** Experimental parameters and the scaling analysis summary

Properties	Experimental Setting 1	Experimental Setting 2
Injection fluid	SAE 85w-140 Gear oil	Water
Fluid viscosity (cP @ 20°C)	1450	1
Flow rate (ml/min)	1	0.1
σ_3 (MPa/Psi)	3.45 MPa (500 Psi)	
σ_2 (MPa/Psi)	8.625 MPa (1250 Psi)	
σ_1 (MPa/Psi)	17.25 MPa (2500 Psi)	
Propagation time (sec) through AE data and far field stress	45	3
κ	1.2	7
Propagation regimes	~Viscosity dominated regime	Toughness dominated regime

366

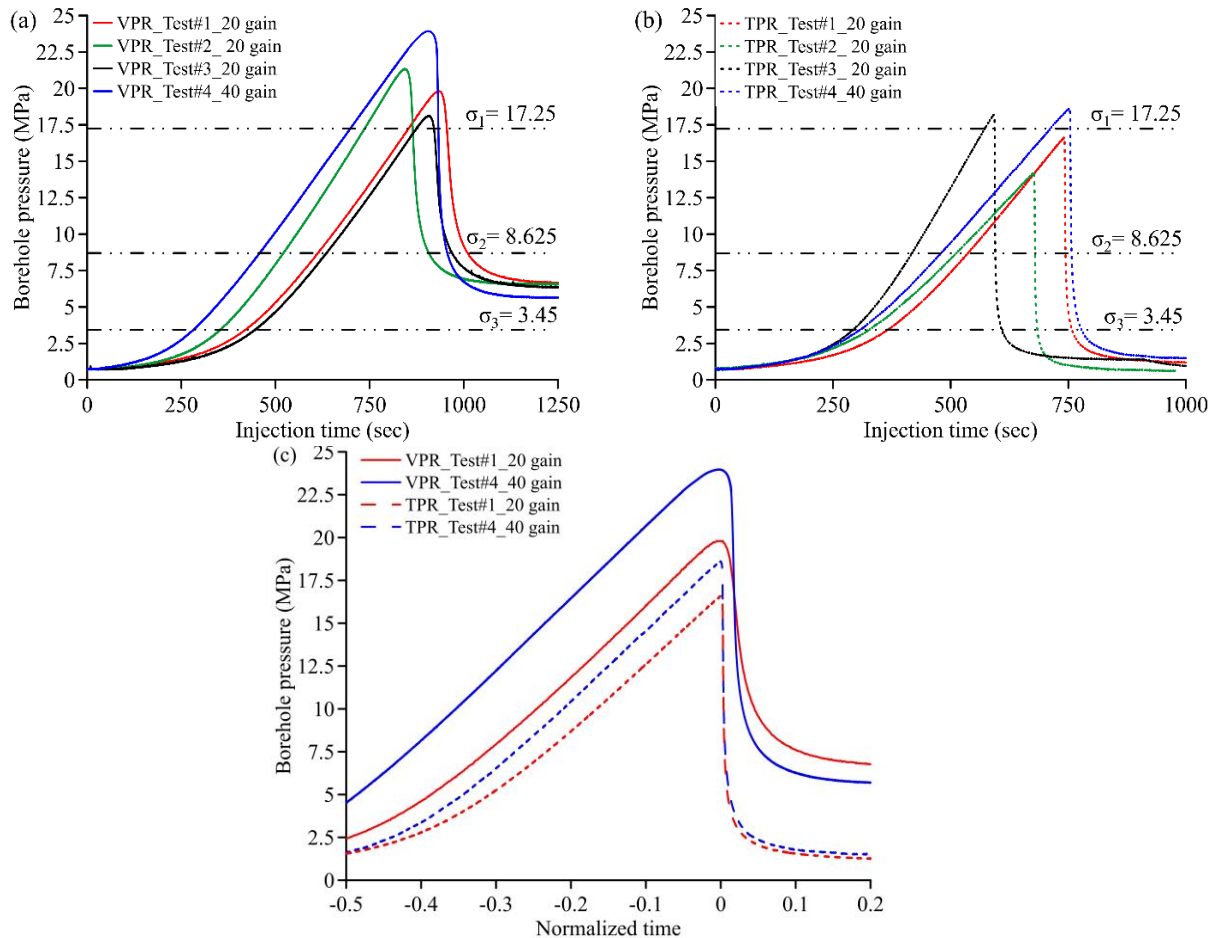
367

368 It is important to emphasize here that the fracture propagation time (time from initiation to
 369 fracture reaching boundaries), which is a significant parameter in the scaling analysis, was
 370 determined using the pressurization rate ($\partial P/\partial t$), detected AEs and the σ_3 stress measurements.
 371 Figure 5 shows the $\partial P/\partial t$, σ_3 stress measurements along with the AEs for VPR_Test#1_20 gain
 372 and TPR_Test#1_20 gain experiments. Fracture initiation was detected earlier by the AE system,
 373 where no change in the borehole pressure, $\partial P/\partial t$ or σ_3 stress could be observed. The fracture
 374 reaching the boundaries of the specimen can be almost deduced from the lowest points of $\partial P/\partial t$,
 375 peak σ_3 stress, and reduction of AEs to a minimal. Overall, the fracture initiation and propagation
 376 coincided well with the increase in the AE rate and σ_3 and the drop in the $\partial P/\partial t$. These propagation
 377 times (Table 1) were quite different from what could be determined through the pressure curve
 378 analysis alone (departure from linearity to a constant value after BP). The same method was used
 379 to determine the fracture propagation time for all other experiments as well.

380

381

382



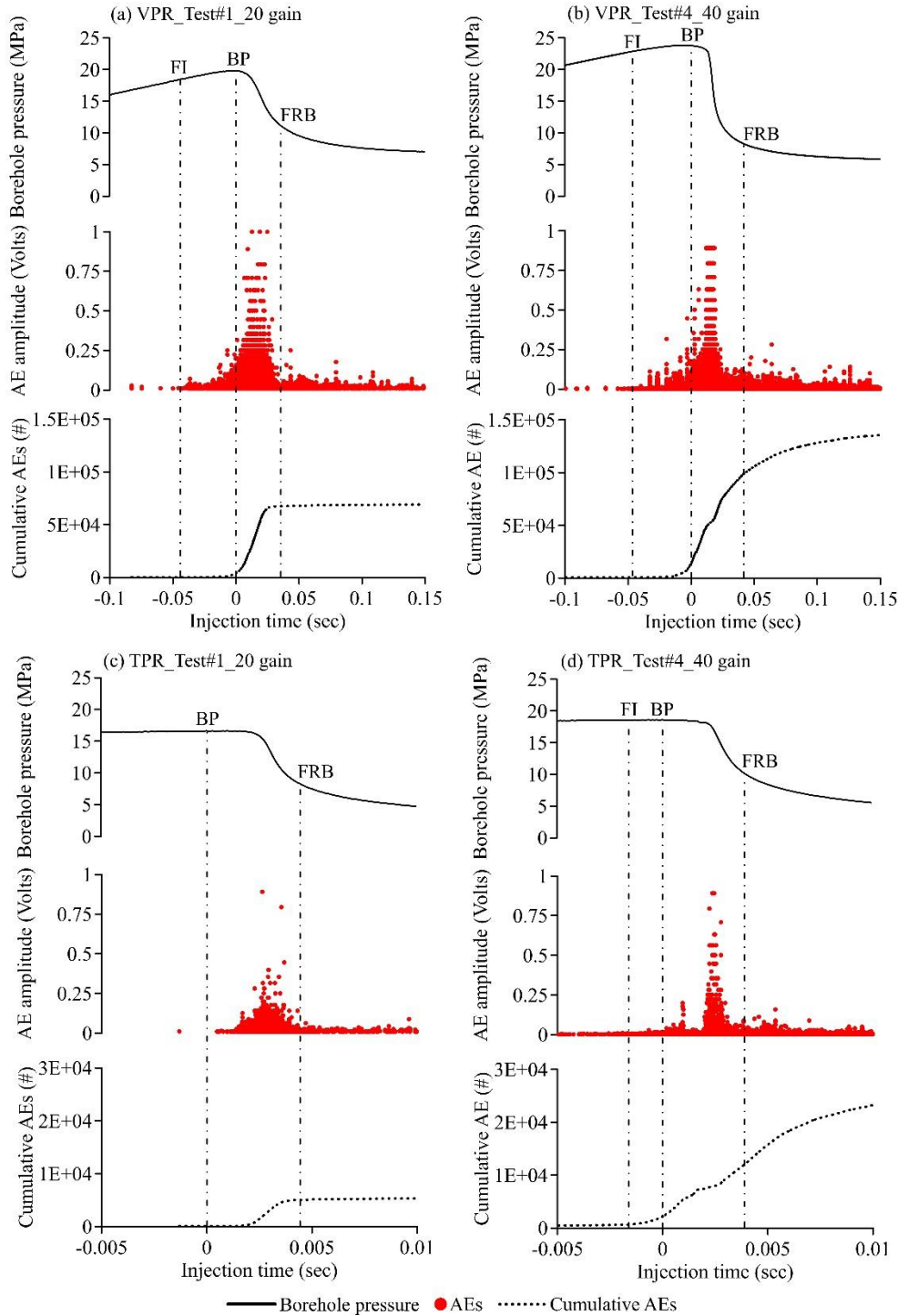
383 **Figure 3.** Borehole pressure evolution with actual experimental time for different (a) VPR and
 384 (b) TPR experiments. (c) Borehole pressure evolution against normalized time for a pair of VPR
 385 and TPR experiments. On average, VPR experiments resulted in higher BPs and gradual pressure
 386 drop after the breakdown, relative to TPR experiments. For all the experiments, the borehole
 387 pressure reached a constant value after breakdown. However, this pressure was higher for VPR
 388 experiments (~6.5 MPa) as compared to the TPR experiments (~1), which represents the ease
 389 with which the injection fluid can excrete out from the generated fracture

390

391

392 Slight differences of 3-4 MPa in the BP for similar experimental conditions were observed
 393 and can be attributed to either the heterogeneities of the rock or the minor differences in the drilled
 394 borehole for different specimens. It can also be deduced from Figure 4 that the pressure decay was
 395 abrupt for experiments conducted with low viscosity fluid and gradual with higher viscosity
 396 injection fluid. This gradually decreasing borehole pressure also allowed for relatively more data
 397 collection time.

398



399

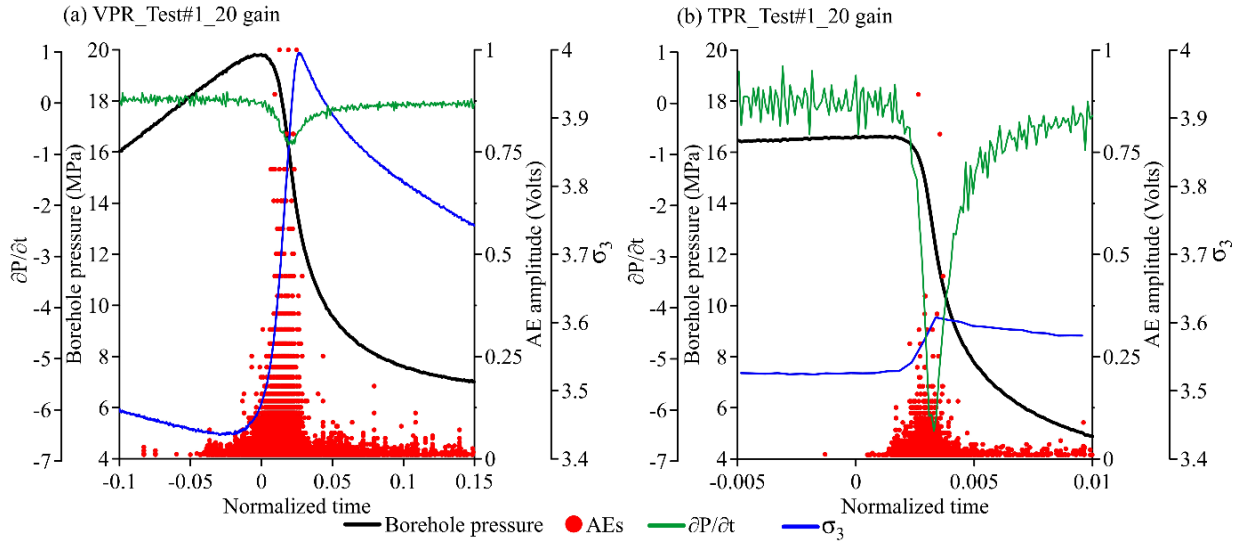
400

401 **Figure 4.** Detected AEs and the cumulative AEs along with the borehole pressure evolution against
 402 normalized time for (a) VPR_Test#1_20 gain, (b) VPR_Test#4_40 gain, (c) TPR_Test#1_20 gain
 403 and (d) TPR_Test#4_40 gain; FI (fracture initiation) represents the point where the AE rate started
 404 to increase, BP (breakdown pressure) was the highest recorded borehole pressure for a particular
 405 experiment, and FRB (fracture reaching boundaries of the specimen) was determined using the
 406 pressurization rate ($\partial P/\partial t$), detected AEs and the σ_3 stress measurements (see figure 5). AEs

407 amplitude from the 40-gain experiment was divided by 10 for comparison with the 20-gain
 408 experiment. The number of AEs detected for VPR and TPR experiments, with 40-gain setting,
 409 were approximately 2 and 7 times higher than those detected with the 20-gain VPR and TPR
 410 experiments, respectively

411

412



413

414 **Figure 5.** Progression of $\partial P/\partial t$ and σ_3 stress with detected AEs for (a) VPR_Test # 1_20 gain and
 415 (b) TPR_Test # 1_20 gain. The peak increase in σ_3 almost coincided with the termination of
 416 significant AE activity for all the experiments. Also, this reduction of AE rate to a minimum
 417 overlapped with the inflection point in $\partial P/\partial t$ as it approached a constant value

418

419

420

421 3.3 Determination of Gutenberg-Richter b-value

422 The frequency-magnitude Gutenberg-Richter (GR), b-value, determines the ratio between
 423 the large and small seismic events and is a fundamental observation in seismology and seismic
 424 risk analysis (Gutenberg & Richter, 1954). The GR distribution relates the number of seismic
 425 events (N) equal to or greater than a given magnitude, to the magnitude of the event (M), as
 426 (Gutenberg & Richter, 1942, 1944, 1956):

$$427 \log(N) = a - b M \quad (3)$$

428

429 where, a and b are constants, which depends on the seismicity rate and properties of the
 430 focal material, respectively (Olsson, 1999). A higher b-value corresponds to a higher frequency of
 431 small magnitude events, whereas a lower b-value points towards the relative abundance of higher
 432 magnitude events. These AE events, which are much more representative of the rock damage
 433 relative to AEs detected by individual sensors, were determined using a minimum of six sensors.

434 The focal amplitude (A_0) of the AE events was determined following Zang et al. (1998) and
 435 McLaskey & Lockner (2014), assuming spherical spreading around a reference sphere of 10 mm.

$$436 \quad A_0 = \sqrt{\frac{1}{k} \sum_{i=1}^k \left(A_i \frac{r_i}{10} \right)^2} \quad (4)$$

437 where k = number of sensors detected the AE event; A_i is the maximum signal amplitude
 438 recorded at the i^{th} sensor; r_i is the distance between source and the i th sensor.

439 In this study, b -values were calculated using the maximum likelihood method described by
 440 Aki (1965), Utsu (1965), and Woessner & Wiemer (2005):

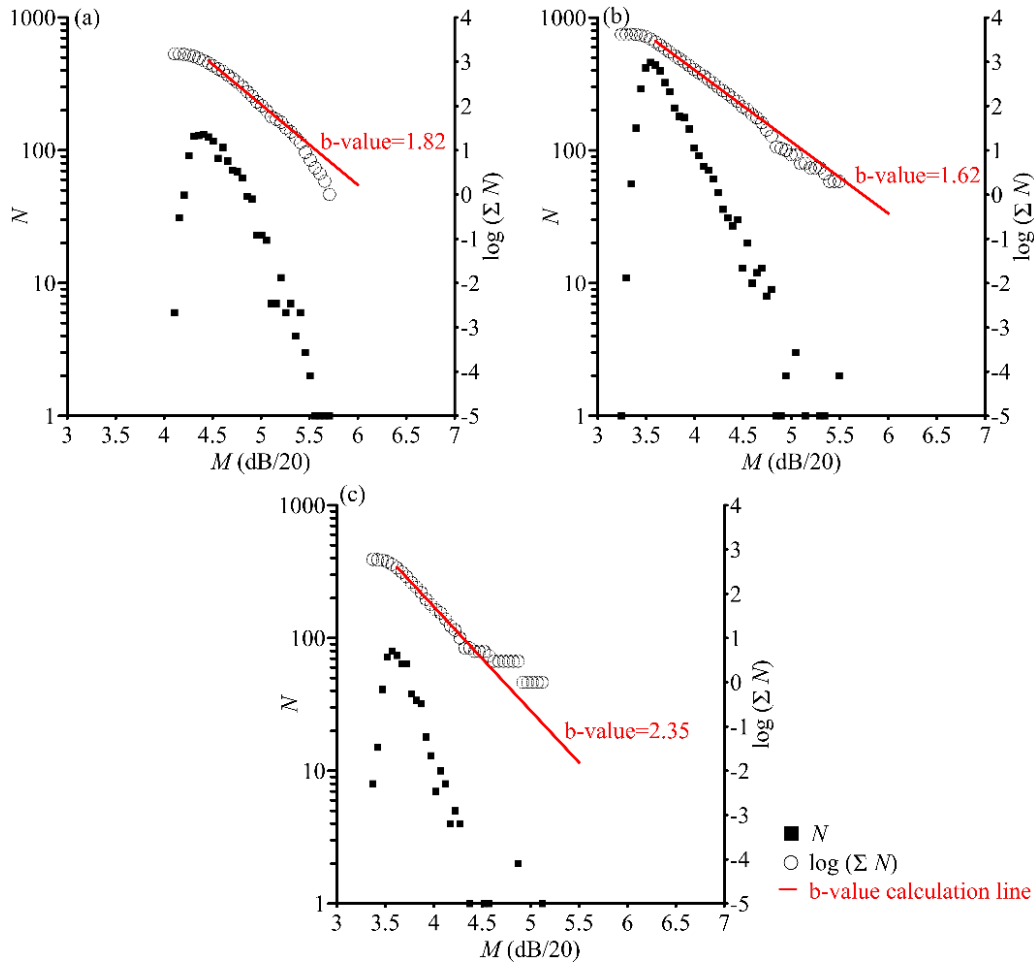
$$441 \quad b = \frac{\log_{10}(e)}{\left[\langle M \rangle - \left(M_c - \frac{\Delta M_{bin}}{2} \right) \right]} \quad (5)$$

442 where, M_c , $\langle M \rangle$ and ΔM_{bin} are the magnitude of completeness, mean magnitude, and
 443 the binning width of the seismic data, respectively. M_c is defined as the lowest magnitude at which
 444 100% of the seismic events can be detected in space and time volume (Rydelek & Sacks, 1989;
 445 Wiemer & Wyss, 2000). In the current study, M_c was determined using Woessner & Wiemer
 446 (2005) method which identifies the point of maximum curvature by computing the maximum value
 447 of the first derivative of the frequency-magnitude curve. This maximum curvature point, taken as
 448 M_c , is a fast estimate which has been reliably and successfully applied to natural earthquakes
 449 sequences (Gulia & Wiemer, 2019), using the slope of the logarithm of the cumulative number of
 450 the detected seismic events, i.e., $\{\log(\sum N)\}$. For the determination of b -value, the AE event
 451 magnitude was obtained by dividing the determined focal amplitude (from Eq 5) in dB by 20,
 452 which also led to the logical selection of 0.05 as the ΔM_{bin} . Figure 6 represents the determined b -
 453 value for both the VPR tests and one TPR test with 40 gain only. The number of AE events (30)
 454 detected for TPR_Test#1_20 gain were insufficient for the b -value analysis.

455 3.4 Spatiotemporal Evolution of AE events

456 The spatiotemporal evolution of AE events inside the rock specimen during the hydraulic
 457 fracturing experiments are presented in Figure 7. In the field, fracture initiates and propagates near
 458 the wellbore plug, which are the zone of stress concentrations (Hampton et al., 2013), whereas in
 459 the laboratory, stress concentration occurs near the top and bottom edges of the open borehole
 460 region. After fracture initiation, HF propagates stably and steadily till BP, which is followed by
 461 the unstable fracture propagation and a rapid decrease in the borehole pressure. In the laboratory
 462 experiments, with finite specimen dimensions, this unstable fracture propagation terminates when
 463 the fracture reaches the boundaries of the specimen. However, even after the fracture reaches the
 464 boundaries of the specimen, some residual fracturing continues till sometime after the borehole
 465 pressure reaches a constant value. Therefore, for all the experiments, the complete propagation of
 466 a hydraulic fracture was divided into three distinct phases: (I) initiation to breakdown, (II)
 467 breakdown to fracture reaching boundaries of the specimen, and (III) the post fracturing phase, till
 468 the end of the experiment. For TPR_Test # 1_20 gain, Figure 7c, AE events were only detected in
 469 phase (II) of the HF experiment.

470



471

472 **Figure 6.** b-value calculation for (a) VPR_Test#1_20 gain, (b) VPR_Test#4_40 gain, and (c)
 473 TPR_Test#4_40 gain experiments. N is the number of seismic events equal to or greater than a
 474 given magnitude (M). M was obtained by dividing the determined focal amplitude in dB by 20 and
 475 ΔM_{bin} was selected as 0.05. The b-value was determined for the linear portion of the $\log(\Sigma N)$
 476 and the M plot

477

478

479

480 Figures 8 and 9 present the complete HF propagation until the termination of the
 481 experiment, marked by the constant borehole pressure and absence of any significant AE activity,
 482 from 3 different views (σ_3 , σ_1 and 3D). The event amplitude, which was normalized as per Eq. (3),
 483 generally increased as the fracture started propagating away from the borehole, as illustrated by
 484 the size of the circles in Figure 8. It can be deduced from these figures 7 - 9 that for VPR
 485 experiments, phases (I) and (III) of HF were clearly and more elaborately identified in the 40-gain
 486 experiment. However, experiment with 20-gain presented a better view of the phase (II) of HF.
 487 For TPR experiments, with much lower input energy (product of fluid viscosity and injection rate),
 488 40 gain presented a much better picture of the HF operation. However, the drawback of the 40 dB
 489 gain setting is that the AE system get saturated during uncontrolled fracturing after breakdown and

490 therefore only able to record the data before and after this unstable fracturing phase, i.e., the sudden
 491 drop in the borehole pressure.

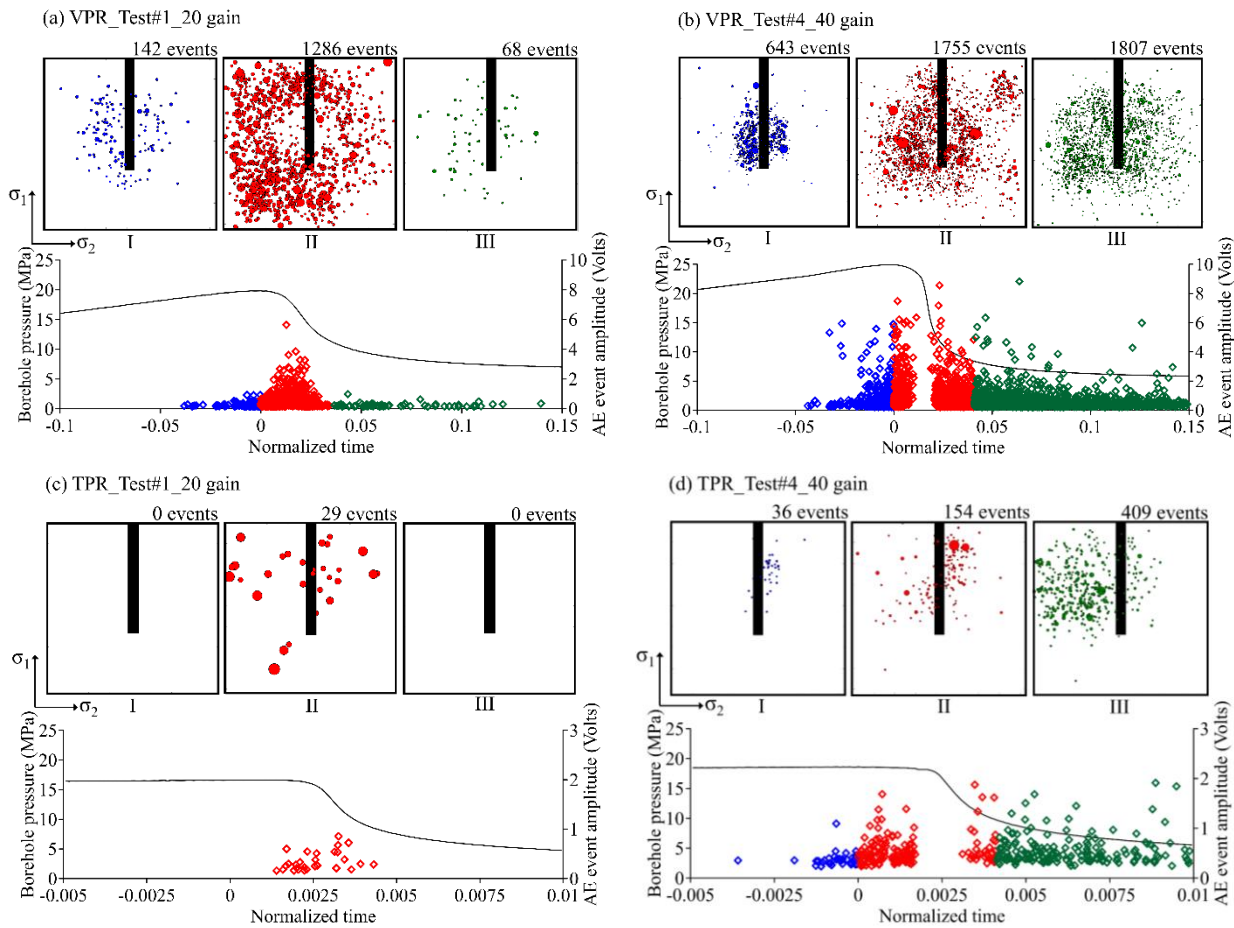
492

493

494

495

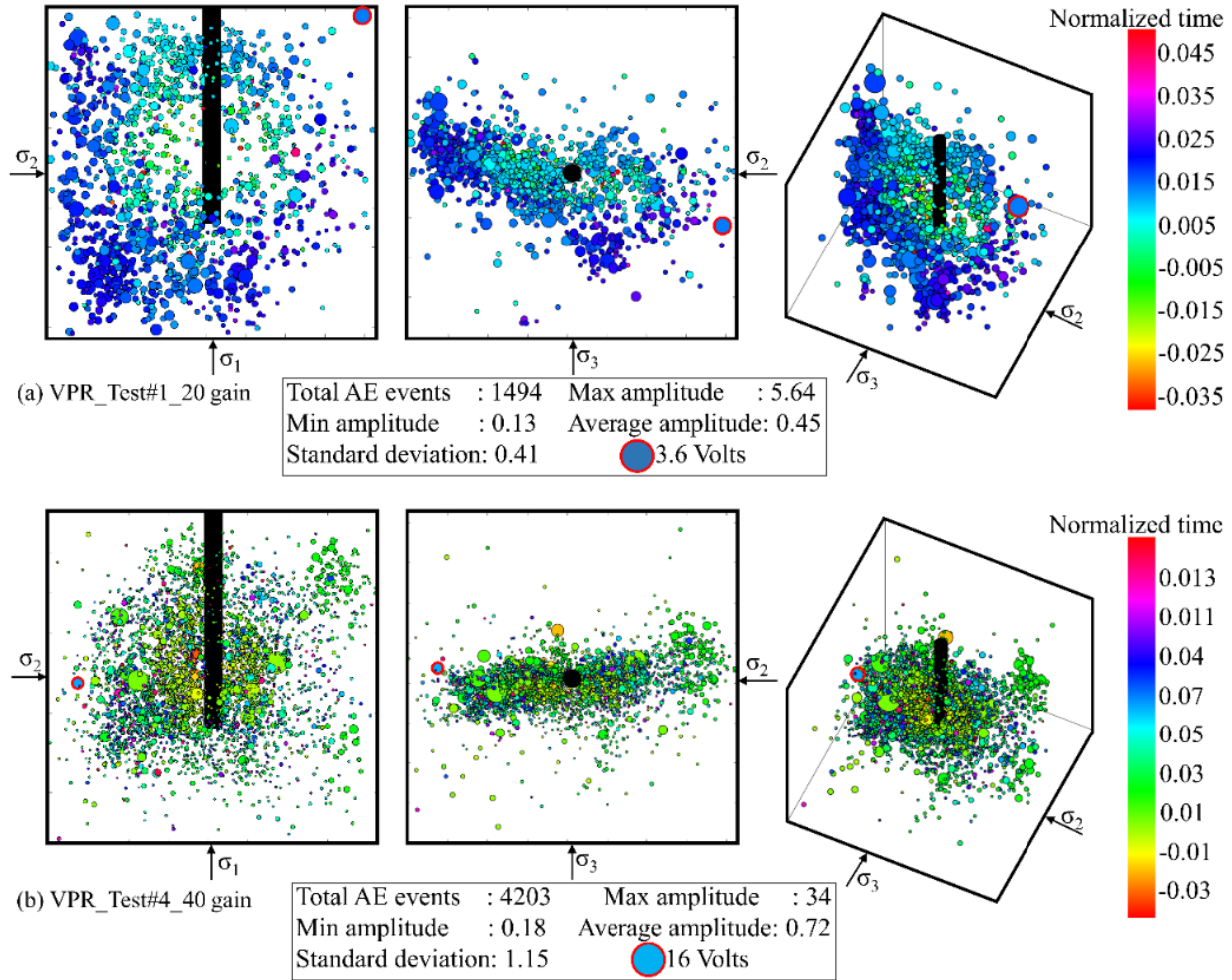
496



497 **Figure 7.** Spatiotemporal evolution of the AE events at different stages of the HF for (a)
 498 VPR_Test#1_20 gain, (b) VPR_Test#4_40 gain, (c) TPR_Test#1_20 gain, and (d)
 499 TPR_Test#4_40 gain; Phase (I) initiation to breakdown, (II) breakdown to fracture reaching
 500 boundaries of the specimen, and (III) the post fracturing phase. The size of the circles represents
 501 the relative AE event amplitude in any particular experiment. The 40-gain experiments were better
 502 at capturing the phase I and the post fracturing phase III periods. AE events were only detected
 503 during phase II for the TPR_Test#1_20_gain experiment

504

505



506

507 **Figure 8.** 2D and 3D view of the complete HF propagation for the (a) VPR_Test#1_20 gain, (b)
 508 VPR_Test#4_40 gain. The HF propagated almost perpendicular to the minimum stress (σ_3) for
 509 both experiments. The occurrence of the AE events with respect to the normalized time is indicated
 510 through the colorbar. Majority of the detected AE events were in the blue and green shade in (a)
 511 and (b), respectively, which indicates that 40-gain setting was able to comprehensively capture the
 512 initial HF portion, whereas the 20-gain was better at identifying the later portion of the HF
 513 propagation

514

515

516

517

3.5 Fracture mechanisms

518

519

520

521

522

523

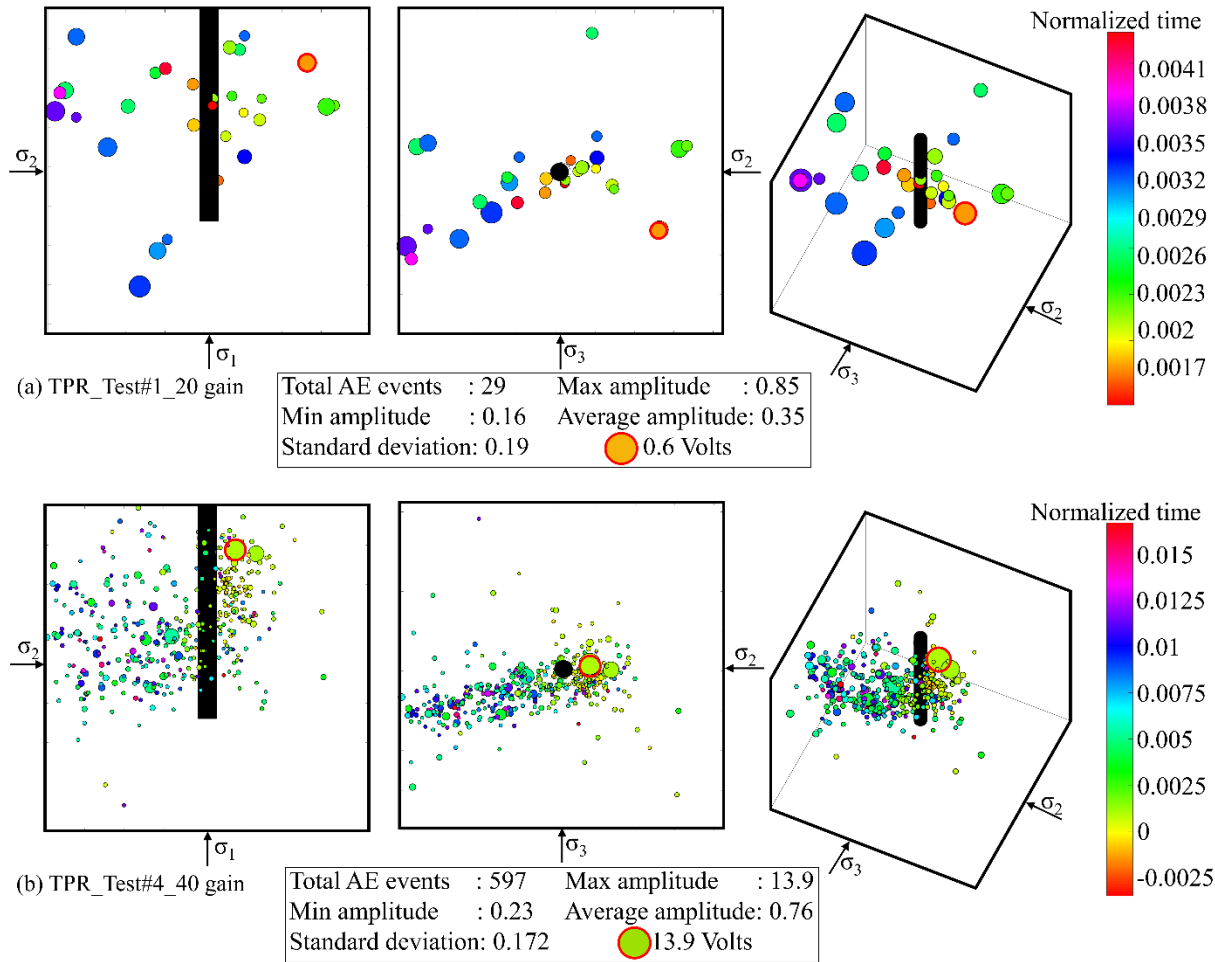
The identification of fracture mechanisms in a hydraulic fracturing operation can inform the hydraulic conductivity of the generated fracture and ultimately the efficiency of the stimulation operation. These damage mechanisms, classified as tensile, shear and mixed mode, along with their orientation, were determined using the MTA and are presented in Figures 10 and 11. The number of AE events for HF experiments with TPR were much lower in number and amplitude for all types of fracture mechanisms. In all the experiments, majority tensile fractures, oriented in

524 the direction of maximum horizontal stress (σ_2) were observed near the borehole and in phase I of
 525 the HF experiment. The percentage of shear and mixed-mode fracture increased in phases II and
 526 III of the HF propagation; however, tensile fracturing still remained as the dominant type for all
 527 the experiments.

528

529

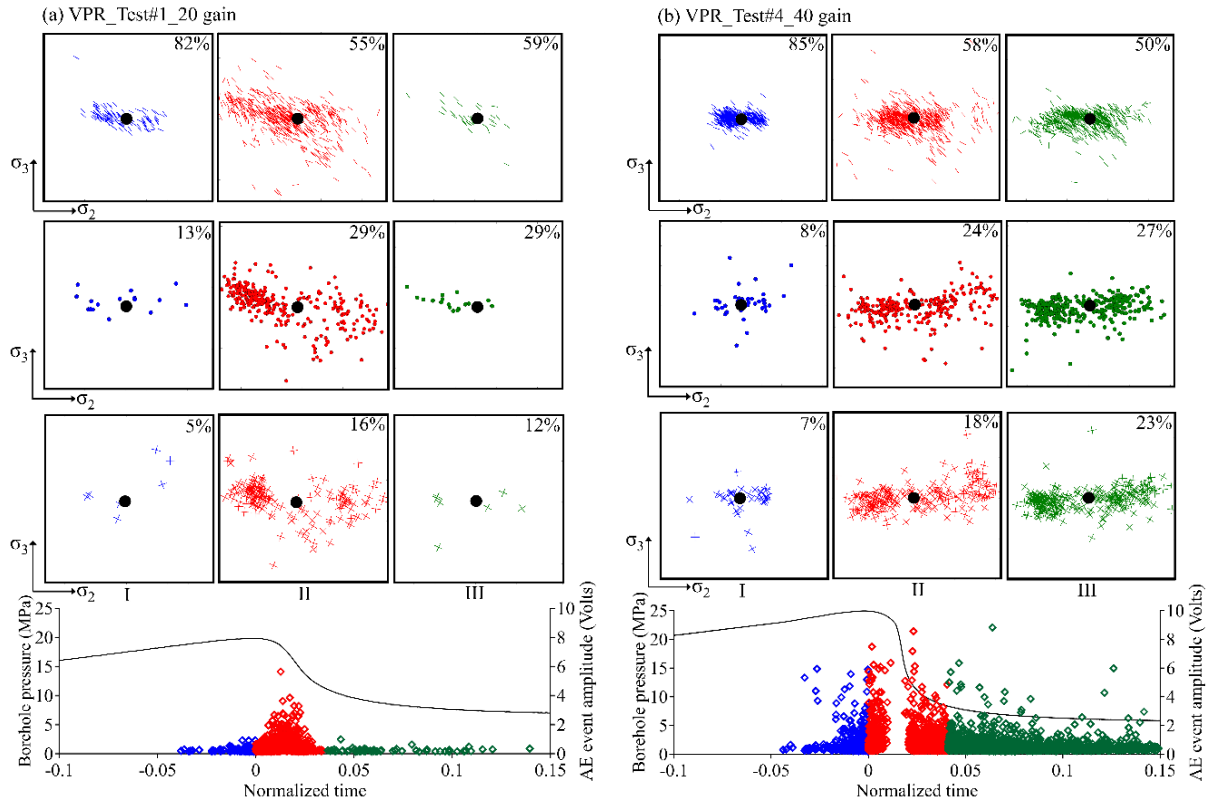
530



531

532 **Figure 9.** 2D and 3D view of the complete HF propagation for (a) TPR_Test#1_20 gain and (b)
 533 TPR_Test#4_40 gain. The occurrence of the AE events with respect to the normalized time is
 534 indicated through the colorbar. In comparison to the VPR experiments, the detected AE events in
 535 the TPR experiments were widely dispersed over the normalized time color spectrum

536



537

538 **Figure 10.** Damage mechanisms determined for different phases for VPR_Test#1_20 gain and (b)
 539 VPR_Test#4_40_gain experiments; tensile, mixed and shear mode in the top, middle and bottom
 540 rows respectively. The percentage of tensile events in the initiation to breakdown phase was
 541 relatively high. However, this percentage decreased as the fracture propagated away from the
 542 borehole

543

544

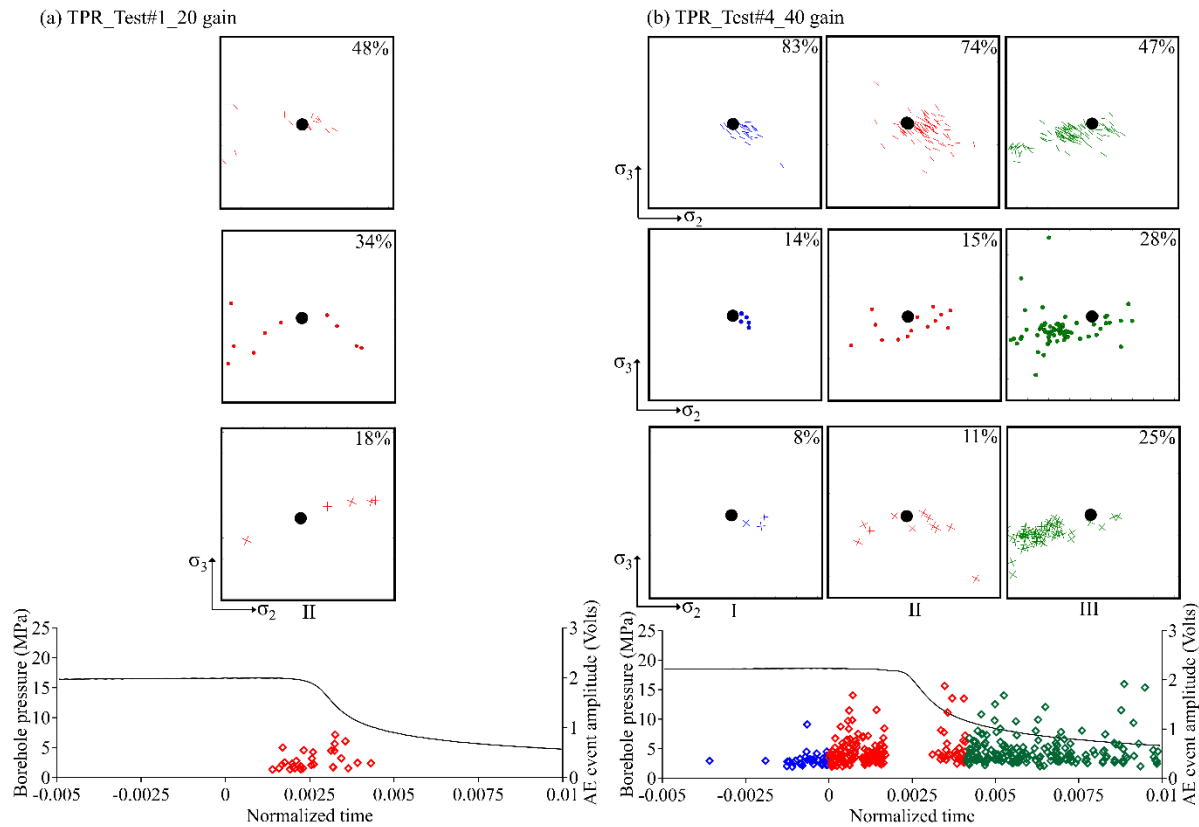
545

546 4 Discussion

547 4.1 Source mechanisms in HF: tensile or shear?

548 In all the experiments of the current study, whether in the VPR or the TPR, tensile
 549 fracturing events were found to be dominating. Hampton et al. (2014) encountered similar results
 550 of about 70.5% tensile in hydraulic fracturing of South Dakota granite. Yamamoto et al. (2019)
 551 observed very strong dominance of tensile fracturing in Kurokami-jima granite, when the rift
 552 (weakest) plane was orthogonal to the fracturing direction. Recently, Naoi et al. (2020) also
 553 experienced similar tensile dominant HF in low permeability eagle ford shale even with low
 554 viscosity injection fluid and concluded that fracturing mechanisms depend on the interaction of
 555 the fracturing fluid and the pre-existing micro-discontinuities. It may be reasonable to believe that,
 556 if the material is impermeable or have very low permeability, the viscosity of the injection fluid
 557 has negligible effects on the fracturing patterns and in that scenario the traditional HF philosophy
 558 could explain the modes of induced seismic events.

559



560

561 **Figure 11.** Damage mechanisms determined for different phases for (a) VPR_Test#1_20_gain and
 562 (b) VPR_Test#4_40_gain experiments; tensile, mixed and shear mode in the top, middle and
 563 bottom rows respectively. AE events were only detected in phase II of the 20-gain experiment (a),
 564 where tensile dominance near the borehole region could be observed. The absence of AE events
 565 pointed towards the saturation of the AE system and the relatively high percentage of tensile events
 566 in phase II of the 40-gain experiment (b).

567

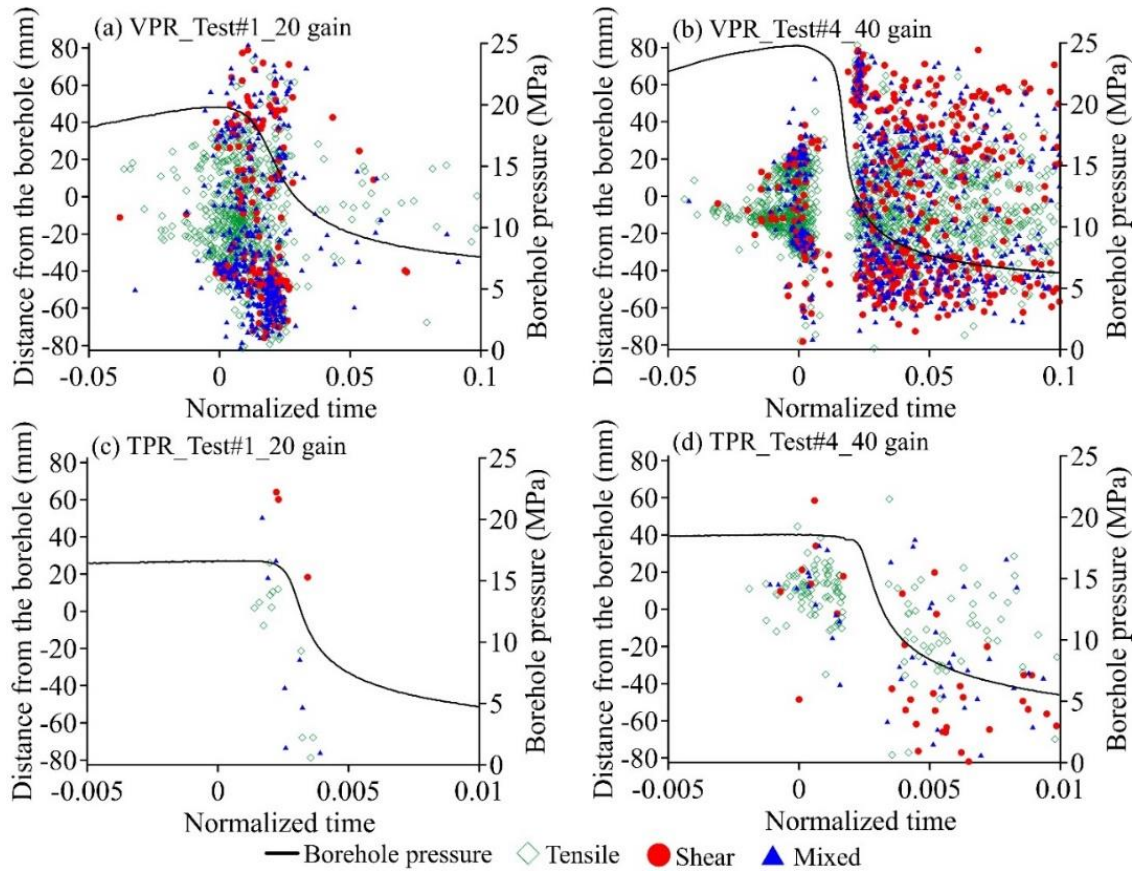
568

569

570 Apart from the early tensile fracturing events dominance, the current study also highlights
 571 how this dominance is reduced as the fracture is propagating away from the injection source. Such
 572 evolution has not been reported in previously conducted HF experiments. Figure 12 presents the
 573 evolution of the fracturing mechanisms from the borehole till the boundaries of the specimen in
 574 the direction of fracture propagation. This varying fracture pattern can be attributed to the pressure
 575 gradient, as the pressure is largest near the injection source (borehole) and decreases as the fracture
 576 propagates away from the borehole. Also, the hydraulic properties of the injection fluid (viscosity
 577 & rate) and the surrounding rock have an increased influence on the fracture propagation away
 578 from the injection source (Stoekhert et al., 2015). All these factors contribute to HF becoming
 579 complex and a combination of different types of fracturing mechanisms as the perimeter of the HF
 580 increases.

581 4.2 Viscosity vs Toughness propagation regime

582 It is important to assess the results from the HF experiments, with respect to their position
 583 in the propagation regime spectrum. The experimental settings used in this study resulted in
 584 drastically different viscosity (or viscosity-transitional) and toughness dominated propagation
 585 regimes, both of which are encountered during the field HF propagation. Table 2 presents a
 586 summary of results for the VPR and TPR experiments. As expected, the VPR experiments, with
 587 higher energy input, resulted in a higher number of AE events and the highest-magnitude event.
 588 On average, the BP and the injected volume were also considerably higher for the VPR
 589 experiments.



590

591 **Figure 12.** Damage mechanisms (tensile, shear, and mixed mode) with distance from the borehole
 592 for (a) VPR_Test#1_20 gain (b) VPR_Test#4_40 gain (c) TPR_Test#1_20 gain and (d)
 593 TPR_Test#4_40 gain. The distance is from the center (0) to the boundaries of the specimen in the
 594 direction of fracture propagation. Relatively more events were detected in the post fracturing phase
 595 by the 40-gain experiments. The absence of events in (b) and (d) for a small period is due to the
 596 saturation of the AE system

597

598 The classical HF models (Nordgren, 1972; Perkins & Kern, 1961) and the scaling analysis
 599 (Detournay, 2004) assume that HF is occurring in mode-I (tensile fracturing). Therefore,
 600 theoretically, the determined propagation regime, either VPR or TPR, should follow this basic
 601 assumption and almost all detected AE events should be tensile fractures. However, as already

602 identified, for all the experiments performed in this study, mostly tensile fractures dominated near
 603 the borehole (75-85%) and both tensile and shear fractures occurred at some distance (20-30 mm)
 604 on either side of the borehole (Figures 12). There can be a number of possible explanations for this
 605 discrepancy between the theoretical expectations and the experimental results. The scaling analysis
 606 calculations assume that the material is completely isotropic, homogeneous, and impermeable,
 607 which can never be the case for a natural rock. Even the micro-flaws in the rock specimen can
 608 have a significant impact on the fracturing patterns, depending on the experimental conditions
 609 (injection fluid / rate). Secondly, this inconsistency may be attributed to the fact that even though
 610 the fluid flow is assumed to be constant throughout the fracturing process, the fluid flow and
 611 consequently the fluid pressure, decreases as the fracture propagates away from the borehole,
 612 depending on the injection rate and also the fluid infiltration in the surrounding rock. Also, when
 613 the perimeter of the HF is small (i.e., at early stages), the energy required to propagate the fracture
 614 is small and viscous flow dominates; however, as this perimeter increases, the required energy also
 615 increases and becomes greater than that required to drive the injection fluid through the fracture
 616 (Lecampion & Desroches, 2015). Therefore, the extent of pure HF (formation of new mode-I
 617 fractures) depends on the pressure losses and the pre-existing faults/discontinuities and might only
 618 be relevant near the borehole region only (Amann et al., 2018). Zhuang & Zang (2021)
 619 hypothesized that for pure viscosity dominated regimes, tensile fractures dominate for the whole
 620 duration of the fracturing operation. However, a pure viscosity dominated regime requires almost
 621 zero penetration of fluid in the surrounding material, which can be achieved only through sleeve
 622 fracturing. For all the other cases, the fractures follow a path from being tensile dominant, near the
 623 borehole, to a combination of fracturing mechanisms, as represented by the results in this study.

624

625 **Table 2.** Summary of results for VPR and TPR experiments

Propagation regime	Test number	BP (MPa)	Injected Volume till BP (ml)	Number of AE events (#)	Maximum amplitude of the AE event (Volts)	b-value	Fracturing mechanisms (%)		
							Tensile	Shear	Mixed
VPR	1	19.8	15.6	1491	5.6	1.82	57.8	14.6	27.6
	4	24.5	14.6	4205	34	1.62	59.2	18.4	22.4
TPR	1	16.6	12.1	30	0.85	*	52.2	13.0	34.8
	4	18.6	11.3	597	14	2.35	56.5	20.2	23.3

626 *b-value was not determined due to insufficient number of determined AE events for
 627 TPR_Test#1_20_gain experiment

628

629 By comparing the fracturing patterns for different experiments, the percentage of tensile
630 fractures decreased with the transition from VPR to TPR, as represented by the slight decrease in
631 overall tensile events between different regime experiments (Figure 9 and 10; Table 2). Even
632 though the viscosity of injection fluid is much lower in the TPR, still it is not low enough to easily
633 penetrate the micro-flaws in Barre granite and cause a drastic difference in the fracturing
634 mechanisms as compared to the VPR experiments. It can be expected that a much lower viscosity
635 fluid (for example, CO₂) may be able to stimulate those micro-size pre-existing discontinuities
636 and present a case where shear fractures are dominant. Also, the fractures created in the VPR, are
637 expected to be planar and smooth with a wider aperture compared to the complex and torturous
638 fractures with more branches, in the toughness domain. This can be confirmed through a micro-
639 structural analysis of the generated HF and is a focus of a future study.

640 The b-value calculated for the two VPR tests and one TPR test was 1.82, 1.62, and 2.35,
641 respectively. A b-value close to unity is normally encountered for natural earthquake sequences.
642 However, Schorlemmer et al. (2005) have suggested that the b-value varies depending on the style
643 of faulting, with highest b-values for normal (tensile) faulting, intermediate values for strike-slip,
644 and lowest for thrust type events. Generally, a b-value of 2 is obtained from the seismicity induced
645 by the main fracturing portion of the field HF operations (Maxwell et al. 2009; Downie et al. 2010).
646 Wessels et al. (2011) observed a b-value of ~2 for seismic events generated as a result of HF in
647 the Barnett shale formation in Ft. Worth Basin, Midcontinent USA. Eaton et al. (2014) calculated
648 the b-value for three different HF projects (Horn river basin, central Alberta, and Cotton valley),
649 with different geological settings. The seismic data from the gas fields resulted in a b-value which
650 varied from 1.63 to 2.61. In the Soultz-sous-Fore^{ts} (Alsace, France) and Basel (Switzerland) EGS
651 projects, Cuenot et al. (2008) and Bachmann et al. (2011) obtained an overall b-value of 1.29 and
652 1.56, respectively. Recently, mine-scale HF experiments at the Aspö Hard Laboratory (Sweden)
653 were carried out to evaluate the applicability of different injection schemes for EGS (Niemz et al.,
654 2020). The cyclic progressive injection scheme resulted in higher b-values (2.34 - 2.51) relative to
655 the conventional continuous injection schemes (1.72-1.95). The b-value determined for the
656 experiments in current study are in line with what should be expected for HF operations. The
657 higher b-value of 2.35 for the TPR experiments indicates the presence of high number of small
658 magnitude events or the absence of large magnitude events, which is expected due to the fact that
659 the energy input and the consequent seismic energy release in TPR experiments is much lower
660 when compared to the VPR experiments.

661

662 4.3 Implications for field HF operations

663 In the field, it is commonly accepted that HF stimulation, in the oil and gas settings
664 (sedimentary rocks), is achieved through the generation and propagation of new fractures (tensile),
665 whereas for the EGS (crystalline rocks), it is achieved through the slipping along the pre-existing
666 fractures (shear) (Economides & Nolte, 1989; McClure & Horne, 2013). However, some
667 researchers (Jung, 2013; McClure, 2012; McClure & Horne, 2014a, 2014b) have argued against
668 this pure shear stimulation supposition for the granitic rocks. They have proposed that HF in
669 granitic rocks contains a much higher percentage of new fracturing than what is believed by the
670 community and is actually a combination of both the tensile fractures and shearing of pre-existing
671 fractures. Observations from large scale HF projects, Fenton Hill EGS (Norbeck et al. 2018) and
672 Sanford Underground Research facility (Schoenball et al. 2020), have also supported this notion
673 of combined type fracturing. Even though the near borehole tensile dominance is not accounted

674 for, the fracturing patterns observed from the experiments in this study, away from the injection
675 source, follows this hypothesized concept. The relatively low percentage of shear fractures, in the
676 current experiments, can be attributed to the almost absence of pre-existing faults/discontinuities,
677 relative to the field.

678 Contrary to the theoretical predictions and the observed laboratory results, the tensile
679 dominance or even a combined type fracturing is rarely observed in the field and shear fracturing
680 is found strongly dominating through the recorded seismic data (Maxwell, 2011a, 2011b). This
681 discrepancy between the laboratory and field scale can be attributed to several factors:

- 682 • First, the material tested in the laboratory is mostly intact without any pre-existing
683 faults/discontinuities. In the field, the rock mass contains numerous fractures of
684 different scales, which can significantly influence the HF propagation. In other
685 words, the experiments performed in the laboratory with intact material represents
686 pure HF experiments, whereas in the field, it can be a combination of both HF and
687 hydro-shearing (HS). This was represented by a small field-scale experimental
688 study (Ishida et al., 2019), which pointed towards initial tensile dominance
689 followed by majority shear fractures as the fracture propagated. Therefore, it can
690 be hypothesized that the stimulation operation can initiate as HF and transitions
691 into a HS mechanism, farther from the injection source.
- 692 • Secondly, factors contributing towards the highlighted inconsistency can be related
693 to the scale of the experiments/operations. The finite sized specimen tested in the
694 laboratory may only be able to replicate only the near borehole phenomena. The
695 increase in shear fractures observed in the current experiments away from the
696 borehole might have even increased to a greater extent if the dimensions of the
697 specimen were not limited. This was also observed in the Basel EGS project (Zhao
698 et al., 2014), where seismic events with significant isotropic components (fracture
699 opening or closing) were found to be dominating only near the injection well.
700 Another drawback of these finite specimen dimensions and the resulting low
701 percentage of shear fractures in the laboratory can be related to the saturation of the
702 AE recording system in the uncontrolled fracturing phase, which is a major portion
703 of HF propagation in the field. The clipped amplitudes (Figure 4b) and long-
704 duration signals (Figures 7b & d), that happen at or just after the BP, overwhelm
705 the AE system and cause system saturation. This is due to the superimposition of
706 many large AEs and their reflections and can result in loss of significant quantity
707 of micro-seismic data. Majority of these missing AE events are expected to be shear
708 fractures, as they are the likely fracture mode at the failure point.
- 709 • Lastly, the extensive and very sensitive AE monitoring from all the sides of the
710 specimen in the laboratory, is almost never possible in the field. Also, a significant
711 portion of the deformation occurring during the HF stimulation is aseismic
712 (Goodfellow et al., 2015a; Villiger et al., 2020), which is also influenced by the
713 distance of the field seismic recording setup from the propagating HF. These
714 conditions may result in a situation where only the high energy seismic events,
715 resulting from the interaction of propagating fractures and pre-existing
716 faults/discontinuities, are detected by the seismic sensors, whereas the relatively
717 low energy tensile events are left undetected.

718 **5 Conclusions**

719 This study focused on controlled laboratory HF of true triaxially loaded crystalline rock
720 cubes with different experimental settings. The selected experimental setting resulted in two
721 drastically different HF propagation regimes: viscosity and toughness dominated propagation
722 regimes. Real-time AE monitoring successfully mapped the generated, almost planar, bi-wing
723 fracture at different instances along the fracture initiation and propagation time, until the fracture
724 reached the specimen boundaries. The main conclusions are presented as follows:

- 725 • VPR experiments were characterized by having higher BPs and injected volume to
726 reach the BP. Also, the released seismic energy (number of AE events and the
727 highest-magnitude event) was found to be greater for the VPR experiments. The
728 low viscosity of injection fluid in the TPR experiments assisted in the relatively
729 easier stimulation of the micro-flaws in granite and consequently resulted in early
730 breakdown of the specimen utilizing a lower volume of the injection fluid.
- 731 • The frequency-magnitude Gutenberg-Richter b-value for the TPR experiments
732 (2.35) was much higher than the VPR experiments (1.62-1.82). These b-values are
733 in line with what is expected for HF operations. Higher b-values for the TPR
734 experiments pointed towards the increased number of low magnitude events and a
735 relatively lower stress perturbation in the damaged region.
- 736 • Overall, tensile dominated fracturing patterns were obtained for both the VPR and
737 TPR experiments, in line with the theoretical expectations of HF in impermeable
738 rocks. This tensile dominance was most pronounced near the injection source and
739 a combination of fracture types were encountered as the perimeter of the HF
740 increased.
- 741 • The scaling law, which assumes tensile HF, may only be applicable near the
742 borehole region. Farther from the borehole, HF propagation follows a path of least
743 resistance, depending on the material strength, pre-existing faults/discontinuities,
744 and is most likely be a combination of different fracturing mechanisms.
- 745 • The released seismic energy is a very small portion of the input hydraulic energy
746 in HF. The laboratory results, with much sensitive and extensive micro-seismic
747 monitoring system, can provide significant information about the HF operation,
748 which may not be available from the field. These results can have important
749 implications in assessment of a HF operation in granite as the fracture pattern and
750 morphology vary depending on the underlying damage mechanism and ultimately
751 decide the permeability increase achieved through the stimulation operation.

752

753 **Acknowledgments**

754 This material is based upon work supported by the U.S. Department of Energy, Office of Basic
755 Energy Sciences, geosciences program under Award Number DE-SC0019117.

756

757

758 **Open Research**

759 The raw and processed data utilized in the preparation of this research article can be accessed through
 760 the private data repository link : <https://figshare.com/s/fe52db679269ec382819>

761

762

763

764

765 **References**

766 Adams, J., & Rowe, C. (2013). Differentiating applications of hydraulic fracturing. In
 767 ISRM International Conference for Effective and Sustainable Hydraulic Fracturing. International
 768 Society for Rock Mechanics and Rock Engineering. <http://dx.doi.org/10.5772/56114>

769 Aki, K. (1965). Maximum likelihood estimate of b in the formula $\log N = a - bM$ and its
 770 confidence limits. *Bull. Earthq. Res. Inst., Tokyo Univ.*, 43, 237-239.

771 Amadei, B., & Stephansson, O. (1997). *Rock stress and its measurement*. Springer Science
 772 & Business Media.

773 Amann, F., Gischig, V., Evans, K., Doetsch, J., Jalali, R., Valley, B., ... & Giardini, D.
 774 (2018). The seismo-hydromechanical behavior during deep geothermal reservoir stimulations:
 775 open questions tackled in a decameter-scale in situ stimulation experiment. *Solid Earth*, 9(1), 115-
 776 137. <https://doi.org/10.5194/se-9-115-2018>

777 Bachmann, C. E., Wiemer, S., Woessner, J., & Hainzl, S. (2011). Statistical analysis of the
 778 induced Basel 2006 earthquake sequence: introducing a probability-based monitoring approach
 779 for Enhanced Geothermal Systems. *Geophysical Journal International*, 186(2), 793-807.
 780 <https://doi.org/10.1111/j.1365-246X.2011.05068.x>

781 Bunger, A. P. (2005). *Near-surface hydraulic fracture* (pp. 3282-3282). Minneapolis, MN:
 782 University of Minnesota. Bunger, A. P., Jeffrey, R. G., & Detournay, E. (2005). Application of
 783 scaling laws to laboratory-scale hydraulic fractures. In *Alaska Rocks 2005, The 40th US*
 784 *Symposium on Rock Mechanics (USRMS)*. American Rock Mechanics Association.

785 Bunger, A. P., & Lecampion, B. (2017). Four critical issues for successful hydraulic
 786 fracturing applications. *Rock mechanics and engineering*, (BOOK_CHAP).

787 Butt, A., Fragomeni, C., Hedayat, A., & Tudisco, E. (2019). Applicability of ultrasonic
 788 tomographic technique for progressive damage evaluation in prismatic rock specimen. In *53rd US*
 789 *Rock Mechanics/Geomechanics Symposium*. American Rock Mechanics Association.

790 Butt, A., Hedayat, A., Tudisco, E., & Roshan, H. (2020). Evaluation of progressive damage
 791 in barre granite using ultrasonic velocity tomography and digital image correlation. In *54th US*
 792 *Rock Mechanics/Geomechanics Symposium*. OnePetro.

- 793 Cheng, Y., & Zhang, Y. (2020). Experimental Study of Fracture Propagation: The
794 Application in Energy Mining. *Energies*, 13(6), 1411. <https://doi.org/10.3390/en13061411>
- 795 Cornet, F. H., Bérard, T., & Bourouis, S. (2007). How close to failure is a granite rock
796 mass at a 5 km depth?. *International Journal of Rock Mechanics and Mining Sciences*, 44(1), 47-
797 66. <https://doi.org/10.1016/j.ijrmms.2006.04.008>
- 798 Cuenot, N., Dorbath, C., & Dorbath, L. (2008). Analysis of the microseismicity induced
799 by fluid injections at the EGS site of Soultz-sous-Forêts (Alsace, France): implications for the
800 characterization of the geothermal reservoir properties. *Pure and Applied Geophysics*, 165(5), 797-
801 828. <https://doi.org/10.1007/s00024-008-0335-7>
- 802 Dai, F. and K.W. Xia. 2013. Laboratory measurements of the rate dependence of the
803 fracture toughness anisotropy of Barre granite. *International Journal of Rock Mechanics and*
804 *Mining Sciences*, 60, pp.57-65. <https://doi.org/10.1016/j.ijrmms.2012.12.035>
- 805 De Pater, C. J., Cleary, M. P., Quinn, T. S., Barr, D. T., Johnson, D. E., & Weijers, L.
806 (1994a). Experimental verification of dimensional analysis for hydraulic fracturing. *SPE*
807 *Production & Facilities*, 9(04), 230-238. <https://doi.org/10.2118/24994-PA>
- 808 De Pater, C. J., Weijers, L., Savic, M., Wolf, K. H. A. A., Van Den Hoek, P. J., & Barr, D.
809 T. (1994b). Experimental study of nonlinear effects in hydraulic fracture propagation (includes
810 associated papers 29225 and 29687). *SPE Production & Facilities*, 9(04), 239-246.
811 <https://doi.org/10.2118/25893-PA>
- 812 Detournay, E. (2004). Propagation regimes of fluid-driven fractures in impermeable rocks.
813 *International Journal of Geomechanics*, 4(1), 35-45. [https://doi.org/10.1061/\(ASCE\)1532-3641\(2004\)4:1\(35\)](https://doi.org/10.1061/(ASCE)1532-3641(2004)4:1(35))
- 815 Detournay, E. (2016). Mechanics of hydraulic fractures. *Annual Review of Fluid*
816 *Mechanics*, 48, 311-339. <https://doi.org/10.1146/annurev-fluid-010814-014736>
- 817 Downie, R. C., Kronenberger, E., & Maxwell, S. C. (2010). Using microseismic source
818 parameters to evaluate the influence of faults on fracture treatments-A geophysical approach to
819 interpretation. In *SPE Annual Technical Conference and Exhibition*. OnePetro.
820 <https://doi.org/10.2118/134772-MS>
- 821 Eaton, D. W., Davidsen, J., Pedersen, P. K., & Boroumand, N. (2014). Breakdown of the
822 Gutenberg-Richter relation for microearthquakes induced by hydraulic fracturing: Influence of
823 stratabound fractures. *Geophysical Prospecting*, 62(4-Vertical Seismic Profiling and
824 *Microseismicity Frontiers*), 806-818. <https://doi.org/10.1111/1365-2478.12128>
- 825 Economides, M. J., & Nolte, K. G. (1989). *Reservoir stimulation (Vol. 2)*. Englewood
826 Cliffs, NJ: Prentice Hall.
- 827 Fallahzadeh, S. H., Hossain, M. M., James Cornwell, A., & Rasouli, V. (2017). Near
828 wellbore hydraulic fracture propagation from perforations in tight rocks: the roles of fracturing
829 fluid viscosity and injection rate. *Energies*, 10(3), 359. <https://doi.org/10.3390/en10030359>
- 830 Garagash, D., & Detournay, E. (2000). The tip region of a fluid-driven fracture in an elastic
831 medium. *J. Appl. Mech.*, 67(1), 183-192. <https://doi.org/10.1115/1.321162>

- 832 Goodfellow, S. D., Nasser, M. H. B., Maxwell, S. C., & Young, R. P. (2015a). Hydraulic
833 fracture energy budget: Insights from the laboratory. *Geophysical Research Letters*, 42(9), 3179-
834 3187. <https://doi.org/10.1002/2015GL063093>
- 835 Goodfellow, S. D., Nasser, M. H. B., Young, R. P., Flynn, J. W., & Reyes-Montes, J. M.
836 (2013). Analysis of continuous acoustic emission waveform records from rock fracturing
837 experiments. In 47th US Rock Mechanics/Geomechanics Symposium. OnePetro.
- 838 Goodfellow, S. D., Tisato, N., Ghofranitabari, M. N. M. H. B., Nasser, M. H. B., & Young,
839 R. P. (2015b). Attenuation properties of Fontainebleau sandstone during true-triaxial deformation
840 using active and passive ultrasonics. *Rock Mechanics and Rock Engineering*, 48(6), 2551-2566.
841 <https://doi.org/10.1007/s00603-015-0833-8>
- 842 Grosse, C. U., & Ohtsu, M. (Eds.). (2008). *Acoustic emission testing*. Springer Science &
843 Business Media.
- 844 Gulia, L., & Wiemer, S. (2019). Real-time discrimination of earthquake foreshocks and
845 aftershocks. *Nature*, 574(7777), 193-199. <https://doi.org/10.1038/s41586-019-1606-4>
- 846 Gutenberg, B., & Richter, C. F. (1942). Earthquake magnitude, intensity, energy, and
847 acceleration. *Bulletin of the Seismological society of America*, 32(3), 163-191.
848 <https://doi.org/10.1785/BSSA0320030163>
- 849 Gutenberg, B., & Richter, C. F. (1944). Frequency of earthquakes in California. *Bulletin*
850 *of the Seismological society of America*, 34(4), 185-188.
- 851 Gutenberg, B., & Richter, C. F. (1954). Frequency and energy of earthquakes. *Seismicity*
852 *of the Earth and Associated Phenomena*, 17-19.
- 853 Gutenberg, B., & Richter, C. F. (1956). Earthquake magnitude, intensity, energy, and
854 acceleration: (Second paper). *Bulletin of the seismological society of America*, 46(2), 105-145.
855 <https://doi.org/10.1785/BSSA0460020105>
- 856 Haimson, B., & Fairhurst, C. (1969). In-situ stress determination at great depth by means
857 of hydraulic fracturing. In *The 11th US symposium on rock mechanics (USRMS)*. OnePetro.
858 <https://www.researchgate.net/publication/254542580>
- 859 Hampton, J., Frash, L., & Gutierrez, M. (2013). Investigation of laboratory hydraulic
860 fracture source mechanisms using acoustic emission. In 47th US Rock Mechanics/Geomechanics
861 Symposium. American Rock Mechanics Association.
- 862 Hampton, J., Gutierrez, M., Matzar, L., Hu, D., & Frash, L. (2018). Acoustic emission
863 characterization of microcracking in laboratory-scale hydraulic fracturing tests. *Journal of Rock*
864 *Mechanics and Geotechnical Engineering*, 10(5), 805-817.
865 <https://doi.org/10.1016/j.jrmge.2018.03.007>
- 866 Hampton, J., Hu, D., Matzar, L., & Gutierrez, M. (2014). Cumulative volumetric
867 deformation of a hydraulic fracture using acoustic emission and micro-CT imaging. In 48th US
868 Rock Mechanics/Geomechanics Symposium. American Rock Mechanics Association.
- 869 Hayashi, K., & Haimson, B. C. (1991). Characteristics of shut-in curves in hydraulic
870 fracturing stress measurements and determination of in situ minimum compressive stress. *Journal*
871 *of Geophysical Research: Solid Earth*, 96(B11), 18311-18321. <https://doi.org/10.1029/91JB01867>

- 872 Hedayat, A., Bobet, A., & Pyrak-Nolte, L. J. (2012). Monitoring slip initiation and
873 propagation along frictional interfaces with seismic wave transmission. In 46th US Rock
874 Mechanics/Geomechanics Symposium. OnePetro.
- 875 Hedayat, A., Haeri, H., Hinton, J., Masoumi, H., & Spagnoli, G. (2018). Geophysical
876 signatures of shear-induced damage and frictional processes on rock joints. *Journal of Geophysical*
877 *Research: Solid Earth*, 123(2), 1143-1160. <https://doi.org/10.1002/2017JB014773>
- 878 Hedayat, A., Pyrak-Nolte, L. J., & Bobet, A. (2014a). Precursors to the shear failure of
879 rock discontinuities. *Geophysical Research Letters*, 41(15), 5467-5475.
880 <https://doi.org/10.1002/2014GL060848>
- 881 Hedayat, A., Pyrak-Nolte, L. J., & Bobet, A. (2014b). Detection and quantification of slip
882 along non-uniform frictional discontinuities using digital image correlation. *Geotechnical Testing*
883 *Journal*, 37(5), 786-799. <https://doi.org/10.1520/GTJ20130141>
- 884 Hedayat, A., Pyrak-Nolte, L. J., & Bobet, A. (2014c). Multi-modal monitoring of slip along
885 frictional discontinuities. *Rock mechanics and rock engineering*, 47(5), 1575-1587.
886 <https://doi.org/10.1007/s00603-014-0588-7>
- 887 Hedayat, A., Pyrak-Nolte, L. J., & Bobet, A. (2014d). Geophysical investigation of shear
888 failure along cohesive-frictional rock discontinuities. In 48th US Rock Mechanics/Geomechanics
889 Symposium. OnePetro.
- 890 Ishida, T. (2001). Acoustic emission monitoring of hydraulic fracturing in laboratory and
891 field. *Construction and Building Materials*, 15(5-6), 283-295. [https://doi.org/10.1016/S0950-](https://doi.org/10.1016/S0950-0618(00)00077-5)
892 [0618\(00\)00077-5](https://doi.org/10.1016/S0950-0618(00)00077-5)
- 893 Ishida, T., Chen, Y., Bennour, Z., Yamashita, H., Inui, S., Nagaya, Y., ... & Nagano, Y.
894 (2016). Features of CO₂ fracturing deduced from acoustic emission and microscopy in laboratory
895 experiments. *Journal of Geophysical Research: Solid Earth*, 121(11), 8080-8098.
896 <https://doi.org/10.1002/2016JB013365>
- 897 Ishida, T., Fujito, W., Yamashita, H., Naoi, M., Fuji, H., Suzuki, K., & Matsui, H. (2019).
898 Crack expansion and fracturing mode of hydraulic refracturing from acoustic emission monitoring
899 in a small-scale field experiment. *Rock Mechanics and Rock Engineering*, 52(2), 543-553.
900 <https://doi.org/10.1007/s00603-018-1697-5>
- 901 Jung, R. (2013). EGS—Goodbye or Back to the Future. In ISRM International Conference
902 for Effective and Sustainable Hydraulic Fracturing. OnePetro.
- 903 Kang, H., Lv, H., Gao, F., Meng, X., & Feng, Y. (2018). Understanding mechanisms of
904 destressing mining-induced stresses using hydraulic fracturing. *International Journal of Coal*
905 *Geology*, 196, 19-28. <https://doi.org/10.1016/j.coal.2018.06.023>
- 906 King, M. S., Pettitt, W. S., Haycox, J. R., & Young, R. P. (2012). Acoustic emissions
907 associated with the formation of fracture sets in sandstone under polyaxial stress conditions.
908 *Geophysical Prospecting*, 60(1), 93-102. <https://doi.org/10.1111/j.1365-2478.2011.00959.x>
- 909 Lecampion, B., & Desroches, J. (2015). Simultaneous initiation and growth of multiple
910 radial hydraulic fractures from a horizontal wellbore. *Journal of the Mechanics and Physics of*
911 *Solids*, 82, 235-258. <https://doi.org/10.1016/j.jmps.2015.05.010>

- 912 Lecampion, B., Desroches, J., Jeffrey, R. G., & Bungler, A. P. (2017). Experiments versus
913 theory for the initiation and propagation of radial hydraulic fractures in low-permeability materials.
914 *Journal of Geophysical Research: Solid Earth*, 122(2), 1239-1263.
915 <https://doi.org/10.1002/2016JB013183>
- 916 Lhomme, T., Detournay, E., & Jeffrey, R. G. (2005). Effect of fluid compressibility and
917 borehole on the initiation and propagation of a transverse hydraulic fracture. *Strength, fracture and*
918 *complexity*, 3(2-4), 149-162.
- 919 Li, B. Q., da Silva, B. G., & Einstein, H. (2019). Laboratory hydraulic fracturing of granite:
920 acoustic emission observations and interpretation. *Engineering Fracture Mechanics*, 209, 200-220.
- 921 Li, B. Q., & Einstein, H. H. (2019). Direct and Microseismic Observations of Hydraulic
922 Fracturing in Barre Granite and Opalinus Clayshale. *Journal of Geophysical Research: Solid Earth*,
923 124(11), 11900-11916. <https://doi.org/10.1029/2019JB018376>
- 924 Liu, D., Lecampion, B., & Blum, T. (2020). Time-lapse reconstruction of the fracture front
925 from diffracted waves arrivals in laboratory hydraulic fracture experiments. arXiv preprint
926 arXiv:2003.13013. <https://doi.org/10.1093/gji/ggaa310>
- 927 Lockner, D. (1993, December). The role of acoustic emission in the study of rock fracture.
928 In *International Journal of Rock Mechanics and Mining Sciences & Geomechanics Abstracts* (Vol.
929 30, No. 7, pp. 883-899). Pergamon. [https://doi.org/10.1016/0148-9062\(93\)90041-B](https://doi.org/10.1016/0148-9062(93)90041-B)
- 930 Lockner, D., & Byerlee, J. D. (1977). Hydrofracture in Weber sandstone at high confining
931 pressure and differential stress. *Journal of Geophysical research*, 82(14), 2018-2026.
932 <https://doi.org/10.1029/JB082i014p02018>
- 933 Mack, M., & Warpinski, N. (2000). Mechanics of Hydraulic Fracturing. In 'Reservoir
934 Stimulation'. (Eds. MJ Economides and KG Nolte) Chapter 9 pp. 9.
- 935 Maxwell, S. C. (2011a). What does microseismicity tells us about hydraulic fractures?. In
936 *SEG Technical Program Expanded Abstracts 2011* (pp. 1565-1569). Society of Exploration
937 Geophysicists. <https://doi.org/10.1190/1.3627501>
- 938 Maxwell, S. C., & Cipolla, C. (2011b). What does microseismicity tell us about hydraulic
939 fracturing?. In *SPE Annual Technical Conference and Exhibition*. OnePetro.
940 <https://doi.org/10.2118/146932-MS>
- 941 Maxwell, S., Goodfellow, S., Lee, B., Mack, M., & Young, R. (2016). Acoustic-emission
942 geomechanics characterization of laboratory hydraulic fracturing. In *2016 SEG International*
943 *Exposition and Annual Meeting*. OnePetro.
- 944 Maxwell, S. C., Jones, M., Parker, R., Miong, S., Leaney, S., Dorval, D., ... &
945 Hammermaster, K. (2009). Fault activation during hydraulic fracturing. In *SEG Technical*
946 *Program Expanded Abstracts 2009* (pp. 1552-1556). Society of Exploration Geophysicists.
947 <https://doi.org/10.1190/1.3255145>
- 948 McClure, M. W. (2012). Modeling and characterization of hydraulic stimulation and
949 induced seismicity in geothermal and shale gas reservoirs (Doctoral dissertation). Stanford
950 University.
- 951 McClure, M. W., & Horne, R. N. (2013). Conditions required for shear stimulation in EGS.
952 In *Proceedings of the 2013 European Geothermal Congress, Pisa, Italy* (Vol. 37).

- 953 McClure, M. W., & Horne, R. N. (2014a). An investigation of stimulation mechanisms in
 954 Enhanced Geothermal Systems. *International Journal of Rock Mechanics and Mining Sciences*,
 955 72, 242-260. <https://doi.org/10.1016/j.ijrmms.2014.07.011>
- 956 McClure, M. W., & Horne, R. N. (2014b). Correlations between formation properties and
 957 induced seismicity during high pressure injection into granitic rock. *Engineering geology*, 175, 74-
 958 80. <https://doi.org/10.1016/j.enggeo.2014.03.015>
- 959 McLaskey, G. C., & Lockner, D. A. (2014). Preslip and cascade processes initiating
 960 laboratory stick slip. *Journal of Geophysical Research: Solid Earth*, 119(8), 6323-6336.
 961 <https://doi.org/10.1002/2014JB011220>
- 962 Naoi, M., Chen, Y., Yamamoto, K., Morishige, Y., Imakita, K., Tsutumi, N., ... &
 963 Kitamura, S. (2020). Tensile-dominant fractures observed in hydraulic fracturing laboratory
 964 experiment using eagle ford shale. *Geophysical Journal International*, 222(2), 769-780.
 965 <https://doi.org/10.1093/gji/ggaa183>
- 966 Nasserli, M. H. B., Mohanty, B., & Young, R. P. (2006). Fracture toughness measurements
 967 and acoustic emission activity in brittle rocks. *Pure and Applied Geophysics*, 163(5-6), 917-945.
 968 <https://doi.org/10.1007/s00024-006-0064-8>
- 969 Niemz, P., Cesca, S., Heimann, S., Grigoli, F., von Specht, S., Hammer, C., ... & Dahm, T.
 970 (2020). Full-waveform-based characterization of acoustic emission activity in a mine-scale
 971 experiment: a comparison of conventional and advanced hydraulic fracturing schemes.
 972 *Geophysical Journal International*, 222(1), 189-206. <https://doi.org/10.1093/gji/ggaa127>
- 973 Norbeck, J. H., McClure, M. W., & Horne, R. N. (2018). Field observations at the Fenton
 974 Hill enhanced geothermal system test site support mixed-mechanism stimulation. *Geothermics*,
 975 74, 135-149. <https://doi.org/10.1016/j.geothermics.2018.03.003>
- 976 Nordgren, R. P. (1972). Propagation of a vertical hydraulic fracture. *Society of Petroleum
 977 Engineers Journal*, 12(04), 306-314. <https://doi.org/10.2118/3009-PA>
- 978 Ohtsu, M. (1995). Acoustic emission theory for moment tensor analysis. *Research in
 979 Nondestructive Evaluation*, 6(3), 169-184. <https://doi.org/10.1007/BF01606380>
- 980 Olsson, R. (1999). An estimation of the maximum b-value in the Gutenberg-Richter
 981 relation. *Journal of Geodynamics*, 27(4-5), 547-552. [https://doi.org/10.1016/S0264-3707\(98\)00022-2](https://doi.org/10.1016/S0264-3707(98)00022-2)
- 982
- 983 Pan, P. Z., Wu, Z. H., Yan, F., Ji, W. W., Miao, S. T., & Wang, Z. (2020). Effect of the
 984 intermediate principal stress on hydraulic fracturing in granite: an experimental study.
 985 *Environmental Earth Sciences*, 79(1), 10. <https://doi.org/10.1007/s12665-019-8760-8>
- 986 Perkins, T. K., & Kern, L. R. (1961). Widths of hydraulic fractures. *Journal of petroleum
 987 technology*, 13(09), 937-949. <https://doi.org/10.2118/89-PA>
- 988 Raaen, A. M., Skomedal, E., Kjørholt, H., Markestad, P., & Økland, D. (2001). Stress
 989 determination from hydraulic fracturing tests: the system stiffness approach. *International Journal
 990 of Rock Mechanics and Mining Sciences*, 38(4), 529-541. [https://doi.org/10.1016/S1365-1609\(01\)00020-X](https://doi.org/10.1016/S1365-1609(01)00020-X)
- 991
- 992 RILEM Technical Committee (Masayasu Ohtsu)**+ 81-96-3423542+ 81-96-3423507
 993 Ohtsu@ gpo. kumamoto-u. ac. jp. (2010). Recommendation of RILEM TC 212-ACD: acoustic

- 994 emission and related NDE techniques for crack detection and damage evaluation in concrete* Test
 995 method for damage qualification of reinforced concrete beams by acoustic emission. *Materials and*
 996 *structures*, 43, 1183-1186.
- 997 Rydelek, P. A., & Sacks, I. S. (1989). Testing the completeness of earthquake catalogues
 998 and the hypothesis of self-similarity. *Nature*, 337(6204), 251-253.
 999 <https://doi.org/10.1038/337251a0>
- 1000 Sano, O., Kudo, Y., & Mizuta, Y. (1992). Experimental determination of elastic constants
 1001 of Oshima granite, Barre granite, and Chelmsford granite. *Journal of Geophysical Research: Solid*
 1002 *Earth*, 97(B3), 3367-3379. <https://doi.org/10.1029/91JB02934>
- 1003 Sarmadivaleh, M. (2012). Experimental and numerical study of interaction of a pre-
 1004 existing natural interface and an induced hydraulic fracture (Doctoral dissertation, Curtin
 1005 University).
- 1006 Sarmadivaleh, M., Joodi, B., Nabipour, A., & Rasouli, V. (2013). Steps to conducting a
 1007 valid hydraulic-fracturing laboratory test. *The APPEA Journal*, 53(1), 347-354.
 1008 <https://doi.org/10.1071/AJ12029>
- 1009 Savic, M., Cockram, M. J., & Ziolkowski, A. M. (1993). Active ultrasonic monitoring of
 1010 laboratory-scale hydraulic fracturing experiments: Numerical modelling vs. experiment. In
 1011 *Offshore Europe*. Society of Petroleum Engineers. <https://doi.org/10.2118/26793-MS>
- 1012 Savitski, A. A., & Detournay, E. (2002). Propagation of a fluid-driven penny-shaped
 1013 fracture in an impermeable rock: asymptotic solutions. *Int. J. Solids Structures*, 39(26), 6311-6337.
 1014 [https://doi.org/10.1016/S0020-7683\(02\)00492-4](https://doi.org/10.1016/S0020-7683(02)00492-4)
- 1015 Schoenball, M., Ajo-Franklin, J. B., Blankenship, D., Chai, C., Chakravarty, A., Dobson,
 1016 P., ... & EGS Collab Team. (2020). Creation of a Mixed-Mode Fracture Network at Mesoscale
 1017 Through Hydraulic Fracturing and Shear Stimulation. *Journal of Geophysical Research: Solid*
 1018 *Earth*, 125(12), e2020JB019807. <https://doi.org/10.1029/2020JB019807>
- 1019 Schorlemmer, D., Wiemer, S., & Wyss, M. (2005). Variations in earthquake-size
 1020 distribution across different stress regimes. *Nature*, 437(7058), 539-542.
 1021 <https://doi.org/10.1038/nature04094>
- 1022 Solberg, P., Lockner, D., & Byerlee, J. D. (1980, February). Hydraulic fracturing in granite
 1023 under geothermal conditions. In *International Journal of Rock Mechanics and Mining Sciences &*
 1024 *Geomechanics Abstracts* (Vol. 17, No. 1, pp. 25-33). Pergamon. [https://doi.org/10.1016/0148-](https://doi.org/10.1016/0148-9062(80)90003-0)
 1025 [9062\(80\)90003-0](https://doi.org/10.1016/0148-9062(80)90003-0)
- 1026 Stanchits, S., Surdi, A., Gathogo, P., Edelman, E., & Suarez-Rivera, R. (2014). Onset of
 1027 hydraulic fracture initiation monitored by acoustic emission and volumetric deformation
 1028 measurements. *Rock Mechanics and Rock Engineering*, 47(5), 1521-1532.
 1029 <https://doi.org/10.1007/s00603-014-0584-y>
- 1030 Stanchits, S., Burghardt, J., & Surdi, A. (2015). Hydraulic fracturing of heterogeneous rock
 1031 monitored by acoustic emission. *Rock Mechanics and Rock Engineering*, 48(6), 2513-2527.
 1032 <https://doi.org/10.1007/s00603-015-0848-1>
- 1033 Stoeckhert, F., Molenda, M., Brenne, S., & Alber, M. (2015). Fracture propagation in
 1034 sandstone and slate—Laboratory experiments, acoustic emissions and fracture mechanics. *Journal*

1035 of Rock Mechanics and Geotechnical Engineering, 7(3), 237-249.
1036 <http://dx.doi.org/10.1016/j.jrmge.2015.03.011>

1037 Utsu, T. (1965). A method for determining the value of " b" in a formula $\log n = a - bM$
1038 showing the magnitude-frequency relation for earthquakes. *Geophys. Bull. Hokkaido Univ.*, 13,
1039 99-103.

1040 Villiger, L., Gischig, V. S., Doetsch, J., Krietsch, H., Dutler, N. O., Jalali, M., ... & Wiemer,
1041 S. (2020). Influence of reservoir geology on seismic response during decameter-scale hydraulic
1042 stimulations in crystalline rock. *Solid Earth*, 11(2), 627-655. [https://doi.org/10.5194/se-11-627-](https://doi.org/10.5194/se-11-627-2020)
1043 2020

1044 Watanabe, N., Egawa, M., Sakaguchi, K., Ishibashi, T., & Tsuchiya, N. (2017). Hydraulic
1045 fracturing and permeability enhancement in granite from subcritical/brittle to supercritical/ductile
1046 conditions. *Geophysical Research Letters*, 44(11), 5468-5475.
1047 <http://dx.doi.org/10.1002/2017GL073898>

1048 Wessels, S., Kratz, M., & De La Pena, A. (2011). Identifying fault activation during
1049 hydraulic stimulation in the Barnett shale: Source mechanisms, b values, and energy release
1050 analyses of microseismicity. In *SEG technical program expanded abstracts 2011* (pp. 1463-1467).
1051 Society of Exploration Geophysicists. <https://doi.org/10.1190/1.3627478>

1052 Wiemer, S., & Wyss, M. (2000). Minimum magnitude of completeness in earthquake
1053 catalogs: Examples from Alaska, the western United States, and Japan. *Bulletin of the*
1054 *Seismological Society of America*, 90(4), 859-869. <https://doi.org/10.1785/0119990114>

1055 Woessner, J., & Wiemer, S. (2005). Assessing the quality of earthquake catalogues:
1056 Estimating the magnitude of completeness and its uncertainty. *Bulletin of the Seismological*
1057 *Society of America*, 95(2), 684-698. <https://doi.org/10.1785/0120040007>

1058 Xie, L., Min, K. B., & Song, Y. (2015). Observations of hydraulic stimulations in seven
1059 enhanced geothermal system projects. *Renewable Energy*, 79, 56-65.
1060 <https://doi.org/10.1016/j.renene.2014.07.044>

1061 Yamamoto, K., Naoi, M., Chen, Y., Nishihara, K., Yano, S., Kawakata, H., ... & Ishida, T.
1062 (2019). Moment tensor analysis of acoustic emissions induced by laboratory-based hydraulic
1063 fracturing in granite. *Geophysical Journal International*, 216(3), 1507-1516.
1064 <https://doi.org/10.1093/gji/ggy493>

1065 Zang, A., Christian Wagner, F., Stanchits, S., Dresen, G., Andresen, R., & Haidekker, M.
1066 A. (1998). Source analysis of acoustic emissions in Aue granite cores under symmetric and
1067 asymmetric compressive loads. *Geophysical Journal International*, 135(3), 1113-1130.
1068 <https://doi.org/10.1046/j.1365-246X.1998.00706.x>

1069 Zhao, P., Kühn, D., Oye, V., & Cesca, S. (2014). Evidence for tensile faulting deduced
1070 from full waveform moment tensor inversion during the stimulation of the Basel enhanced
1071 geothermal system. *Geothermics*, 52, 74-83. <https://doi.org/10.1016/j.geothermics.2014.01.003>

1072 Zhuang, L., Kim, K. Y., Jung, S. G., Diaz, M., & Min, K. B. (2019a). Effect of water
1073 infiltration, injection rate and anisotropy on hydraulic fracturing behavior of granite. *Rock*
1074 *Mechanics and Rock Engineering*, 52(2), 575-589. <https://doi.org/10.1007/s00603-018-1431-3>

1075 Zhuang, L., Kim, K. Y., Jung, S. G., Diaz, M., Min, K. B., Zang, A., et al. (2019b). Cyclic
1076 hydraulic fracturing of pocheon granite cores and its impact on breakdown pressure, acoustic
1077 emission amplitudes and injectivity. *International Journal of Rock Mechanics and Mining*
1078 *Sciences*, 122, 104065. <https://doi.org/10.1016/j.ijrmms.2019.104065>

1079 Zhuang, L., Kim, K. Y., Shin, H. S., Jung, S. G., & Diaz, M. (2018). Experimental
1080 investigation of effects of borehole size and pressurization rate on hydraulic fracturing breakdown
1081 pressure of granite. In *ISRM International Symposium-10th Asian Rock Mechanics Symposium*.
1082 *International Society for Rock Mechanics and Rock Engineering*.

1083 Zhuang, L., & Zang, A. (2021). Laboratory hydraulic fracturing experiments on crystalline
1084 rock for geothermal purposes. *Earth-Science Reviews*, 103580.
1085 <https://doi.org/10.1016/j.earscirev.2021.103580>

1086 Zoback, M. D., Rummel, F., Jung, R., & Raleigh, C. B. (1977). Laboratory hydraulic
1087 fracturing experiments in intact and pre-fractured rock. In *International Journal of Rock Mechanics*
1088 *and Mining Sciences & Geomechanics Abstracts* (Vol. 14, No. 2, pp. 49-58). Pergamon.
1089 [https://doi.org/10.1016/0148-9062\(77\)90196-6](https://doi.org/10.1016/0148-9062(77)90196-6)